ABSTRACT

HEAT TRANSFER MODEL FOR THE IGNITION
OF METAL POWDER ON A HEATED FILAMENT

by
Trent Stanton Ward

The thermal processes leading to ignition of metal powders in environments that experience rapid temperature changes are currently poorly understood. In this research, a methodology for studying and quantification of such processes is developed. In the experimental case study, the ignition temperature of Mg powder coated on the surface of an electrically heated filament is detected optically at different heating rates. To interpret the results, a heat transfer model has been developed for a multilayer powder coating on top of an electrically heated filament. The coating is modeled using a hexagonal close packed geometry and the heat transfer equations are derived for one dimensional heat flow. An Arrhenius type expression is used to describe the chemical reaction leading to ignition with the pre-exponent as an adjustable parameter. The contact resistance between each powder layer was derived using the bulk thermal properties of the powder. The thermal diffusivity of the powder was measured using the laser flash diffusivity technique for a powder sample freely loaded in a thin cylindrical cavity made in a heat insulator. The pre-exponent identified by matching the computations with the experimental data is 1×10^{10} kg/m^{2}s. For the Mg powder, it is concluded that the thermal processes leading to ignition, for a range of heating rates between 90 and 16,000 K/s, can be described by a single Arrhenius expression. In general, the developed methodology was validated can now be used for studying ignition of different reactive powders.

HEAT TRANSFER MODEL FOR THE IGNITION OF METAL POWDER ON A HEATED FILAMENT

by

Trent Stanton Ward

A Thesis
Submitted to the Faculty of
New Jersey Institute of Technology
in Partial Fulfillment of the Requirements for the Degree of
Master of Science in Mechanical Engineering

Department of Mechanical Engineering

May 2005

Blank Page

APPROVAL PAGE

HEAT TRANSFER MODEL FOR THE IGNITION
OF METAL POWDER ON A HEATED FILAMENT

Trent Stanton Ward

Dr. Edward L. Dreizin, Thesis Advisor   Date
Professor of Mechanical Engineering, NJIT

Dr. Rajesh N. Dave, Committee Member   Date
Professor of Mechanical Engineering, NJIT

Dr. Mirko Schoenitz, Committee Member   Date
Assistant Research Professor of Mechanical Engineering, NJIT

BIOGRAPHICAL SKETCH

Author: Trent Stanton Ward

Degree: Master of Science

Date: May 2005

Undergraduate and Graduate Education:

- Master of Science in Mechanical Engineering,
  New Jersey Institute of Technology, Newark, NJ, 2005

- Bachelor of Science in Mechanical Engineering,
  New Jersey Institute of Technology, Newark, NJ, 2005

Major: Mechanical Engineering

Presentations and Publications:

Ward, T. S., Trunov, M., & Dreizin, E. L. (2005). Heat Transfer Model for Ignition of
     Metal Powder on a Heated Filament. *Proceedings of the 2005 Joint Meeting of the
     U.S. Sections of The Combustion Institute.* Philadelphia, Pennsylvania. March 20-
     23.

Ward, T. S., Chen, W., Schoenitz, M., Dreizin, E. L., & Dave, R. N. (2005). A Study of
     Mechanical Alloying Processes using Reactive Milling and Discrete Element
     Modeling. *Acta Materialia,* (accepted, March 2005).

Ward, T. S., Chen, W., Schoenitz, M., Dreizin, E. L., & Dave, R. N. (2005). Nano-
     Composite Energetic Powders Prepared by Arrested Reactive Milling. *AIAA
     paper,* 2005-0136.

Schoenitz, M., Ward, T. S., & Dreizin, E. L. (2004). Preparation of Energetic Metastable
     Nano-Composite Materials by Arrested Reactive Milling. *Materials Research
     Society Proceedings,* 800, AA2.6.1-AA2.6.6.

Schoenitz, M., Ward, T. S., & Dreizin, E. L. (2005). Fully Dense Nano-Composite
     Energetic Powders Prepared By Arrested Reactive Milling. *Proceedings of The
     Combustion Institute,* 30, 2071-2078.

Chen, W., Schoenitz, M., Ward, T. S., Dave, R. N, & Dreizin, E. L. (2004). Numerical Simulation of SPEX Reactive Milling System by Discrete Element Method. *Proceeding of the Eleventh International Conference on Composites/Nano Engineering*, Hilton-Head, South Carolina. August 8-14.

Schoenitz, M., Ward, T. S., & Dreizin, E. L. (2005). Arrested Reactive Milling for In-Situ Production of Energetic Nanocomposites for Propulsion and Energy-Intensive Technologies in Exploration Missions. *AIAA paper*, 2005-0717.

Bazyn, T., Glumac, N., Krier, H., Ward, T. S., Schoenitz, M., & Dreizin, E. L. (2005). Reflected Shock Ignition and Combustion of Aluminum and Nanocomposite Thermite Powders. *Combustion Science and Technology,* (submitted, March 2005).

Dreizin, E. L., Schoenitz, M., Shoshin, Y. L., Trunov, M. A., Umbrajkar, S., Ward, T. S., & Zhu, X. (2005). Highly-Energetic Nanocomposite Powders Produced by Arrested Reactive Milling. *Proceedings of 36th International Annual Conference of ICT combined with 32nd International Pyrotechnics Seminar,* Karlsruhe, Germany. June 28 - July 1.

To my wife, Jennifer

ACKNOWLEDGMENT

I would like to express my deepest appreciation to Dr. Edward Dreizin for serving as my undergraduate and graduate research advisor. I will always be indebted to Dr. Dreizin because of the constant insight, support, direction, and priceless resources he provided, all of which made my graduate study possible. Special thanks are given to Dr. Rajesh Dave and Dr. Mirko Schoenitz for actively participating in my committee and providing valuable feedback.

I would like to extend my gratitude to Dr. Schoenitz who was instrumental in my research. I owe much of my success to Dr. Schoenitz because of his commitment and expertise. I would like to acknowledge Dr. Dave and Dr. Pfeffer for obtaining my graduate funding. Thanks are given to the National Science Foundation and the Office of Naval Research for providing the NSF-Navy Civilian Service Fellowship.

The staff and students of the Energetic Materials Laboratory also deserve recognition for their valuable support and consultation. I'm especially grateful to Mikhaylo Trunov whose ideas and direction were the foundation of this project.

TABLE OF CONTENTS

LIST OF TABLES

LIST OF FIGURES

CHAPTER 1

INTRODUCTION

1.1 Objective

The objective of this thesis is to develop a methodology for identification of ignition for metal particles in environments where the temperature changes rapidly. The methodology includes an experimental technique and a theoretical model describing ignition of metal powders in the specific experimental configuration. A specific objective of this project is to validate the developed methodology for a case study using spherical magnesium powder. The activation energy of magnesium oxidation has been reported in the literature and the Arrhenius pre-exponent factor describing the chemical kinetics leading to ignition will be determined.

1.2 Background

Metal based fuels are widely used in propellants, explosives, and pyrotechnics because of their high combustion enthalpies. The most significant limitation of metal fuels is associated with the relatively low overall reaction rates. Specifically, reducing the ignition delay time, which can be defined as the period when the metal particle is introduced in the combustion system and represents a heat sink rather than a heat source, is an important challenge. Analysis of reaction kinetics combined with a heat transfer model enables one to introduce a concept of ignition temperature. This temperature is often defined as the lowest temperature of the environment at which the particle would self-heat and start burning [1,2]. This definition is adequate for slow ignition processes

in situations where no pronounced changes in the temperature of the environment occur. In propellants and explosives, however, the temperature of a fuel particle's environment changes rapidly and can exceed the classic ignition temperature before the particle can be considered as a heat source. Thus, a different definition of the ignition temperature, as a temperature reached by the particle in order to become a heat source, is often used in the models describing practical reactive systems. Because of the reaction kinetics, the ignition temperature defined above increases as the environment heating rate increases, but comparison between results is difficult because of significant differences in the dimensions and shapes of the samples, in the experimental heating rates, and in the types of indicators used to identify ignition. A quantitative model describing the ignition kinetics of metal-based fuels is needed to understand which material or geometric properties affect ignition, and to implement in subsequent combustion modeling of metallic fuels.

Several experimental techniques such as a shock tube [3-5] and heated filament [6-8] are used to study the ignition temperature of metal-based fuels. A review of common experimental methods for studying aluminum ignition is given in Reference [9]. In shock tubes, the metal particles are dispersed and heated stepwise by varying the shockwave Mach number [3]. In heated filament ignition experiments, a coating of metal powder is placed on a filament and the filament heating rate is varied by adjusting the electric current [6,7]. In both experiments, optical diagnostics determine the ignition delay time, and the ignition temperature can be estimated. The ignition model described in this thesis is based on the heated filament ignition experiments.

Previously, to describe the heated filament experiment, a heat transfer model was developed for a monolayer of particles coating the filament [10]. The particle layer is therefore directly heated through conduction from the filament and cooled by the environment. The model treated the contact resistance between the filament and powder layer as an adjustable parameter. The simplifying assumptions made in that model resulted in predicted ignition temperatures that only marginally described the experimental data. It is hypothesized that the actual heat transfer processes in the multilayer coating significantly affect the ignition temperature and need to be considered.

As in the earlier model [10], the model developed here considers heat transfer from the filament to the coating, and the heat transfer through the coating to the surrounding. The new primary challenge in the model is to describe the heat transfer through the powder coating. The contact resistance between individual powder particles is determined from the bulk thermal properties of a powder, which were measured using the flash method [11]. The flash method is a technique commonly used to determine the thermal diffusivity of metals and was adapted for application to metal powder.

The heat generated by the chemical reaction between the metal fuel and oxidizer is treated using an Arrhenius type rate expression. The experimental conditions are directly modeled and the powder coating temperature history is calculated until the ignition instant is recognized; the ignition temperature is determined as the filament temperature at this ignition instant.

Spherical magnesium powder was used as the test case for the experiments and model calculations. Magnesium was chosen because its kinetics are well known [4,10,12,13] and because of some practical applications as an additive to propellants and

pyrotechnics [14]. The ignition temperatures of magnesium are also fairly low and fall in the measurable range of the heated filament ignition experiment. Using spherical particles of Mg simplifies the description of the multilayer coating geometry. The goal of the ignition model is to lump multiple processes that occur during ignition of a metal powder into one Arrhenius term and determine that term based on the experimental data. For the model validation, the case study of magnesium enables one to use the activation energy from the literature [10]. Therefore, only the pre-exponent needs to be considered as an adjustable parameter optimized to fit the experimental data.

The motivation of this work is to identify how the pre-exponent factor and the ignition kinetics are affected by a number of parameters such as the powder particle size and the number of layers coating the filament. From these observations, a pre-exponent factor will be found that will characterize the ignition delay of the material for a given range of heating rates. Upon validation of the model using the Mg experiments, the model can be adapted for other powdered fuels so that kinetics data on ignition can be predicted. Such data will be useful in the modeling of explosives and propellants that use metal-based fuels as additives to improve combustion performance.

CHAPTER 2

HEATED FILAMENT IGNITION EXPERIMENT

2.1 General Description

The heated filament ignition experiment is a technique to determine the ignition kinetics of metal powders. In this experiment, the environment temperature at which the particle ignites is determined for various environment heating rates. From the ignition instant and environment heating rate, the ignition kinetics leading to ignition can be established. The filament is heated electrically with a heating rate that can vary between 90 K/s and 16,000 K/s. The filament temperature is measured using infrared pyrometry and the ignition instant is determined by photometry. The ignition instant is determined from the spike in radiation emitted by the burning powder and the ignition temperature is the filament temperature at the corresponding time. A detailed description of the experimental setup follows below.

2.2 Magnesium Powder Characterization

The spherical Mg powder is from Hart Metals, Inc., and is 98% pure. The particle sizes of the powder were measured by Low Angle Laser Light Scattering using a Coulter LS 230 Enhanced Laser Diffraction particle size analyzer. For these measurements, the powder was dispersed in ethylene glycol. The size distribution for the spherical Mg powder is shown in Figure 2.1. The volumetric mean particle diameter is 9.7±5.9 μm.

A Scanning Electron Microscope (SEM) was used to observe the morphology of the Mg powder and a typical SEM image is shown in Figure 2.2. From the micrograph,

the morphology is near spherical and the particle size range is consistent with the particle size analysis shown in Figure 2.1. A few crystalline particles and some rough texture on the Mg surface is a combination of MgO and $Mg(OH)_2$ due to exposure to the atmosphere.
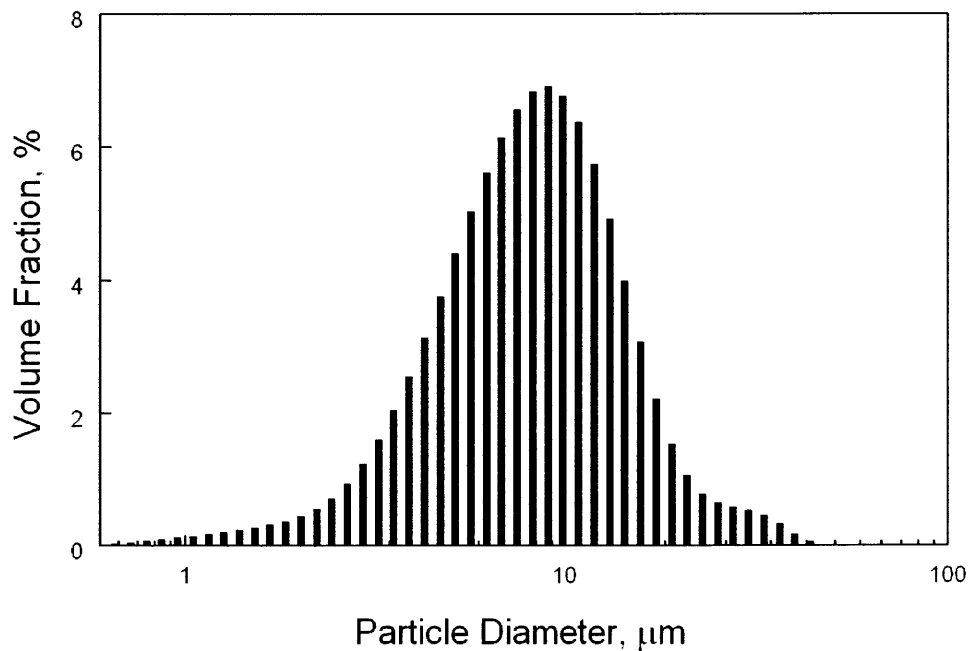
Figure 2.1 Particle size distribution for spherical Mg powder investigated.
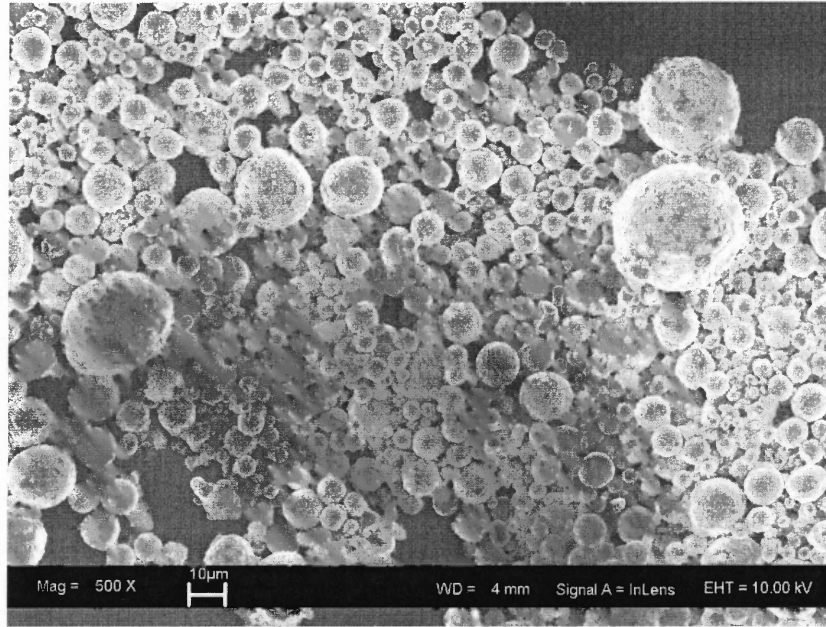
Figure 2.2 Micrograph of Mg powder showing morphology and surface effects.

2.3 Experimental Apparatus and Procedure

The experimental setup has two key elements including the electrical circuitry to heat the filament and the diagnostics to determine the ignition instant and ignition temperature. The apparatus is illustrated schematically in Figure 2.3. The electrical circuit consists of one loop with the voltage supplied by one or two 12V car batteries connected in series, a resistance box to control the current, and the filament. In these experiments, the filament was Nickel-Chromium; however, a carbon substrate can be used to attain higher temperatures that might be needed to ignite such metals as aluminum. The temperature of the uncoated portion of the filament is measured in real time using a high-speed infrared optical pyrometer. The pyrometer detector is model OS1581 and the monitor is model DP1581 from Omega Engineering, Inc. A high-speed photo detector is focused on the powder and is used to measure the radiation emitted by the burning powder. The

photo detector is a silicon based photodiode with a spectral range between 350-1100 nm; it is model DET110 from Thorlabs. The data acquisition system used to monitor the pyrometer and photo detector signals is a National Instruments BNC-2110 multi-channel board and a PCI-MIO-16E-4 card.
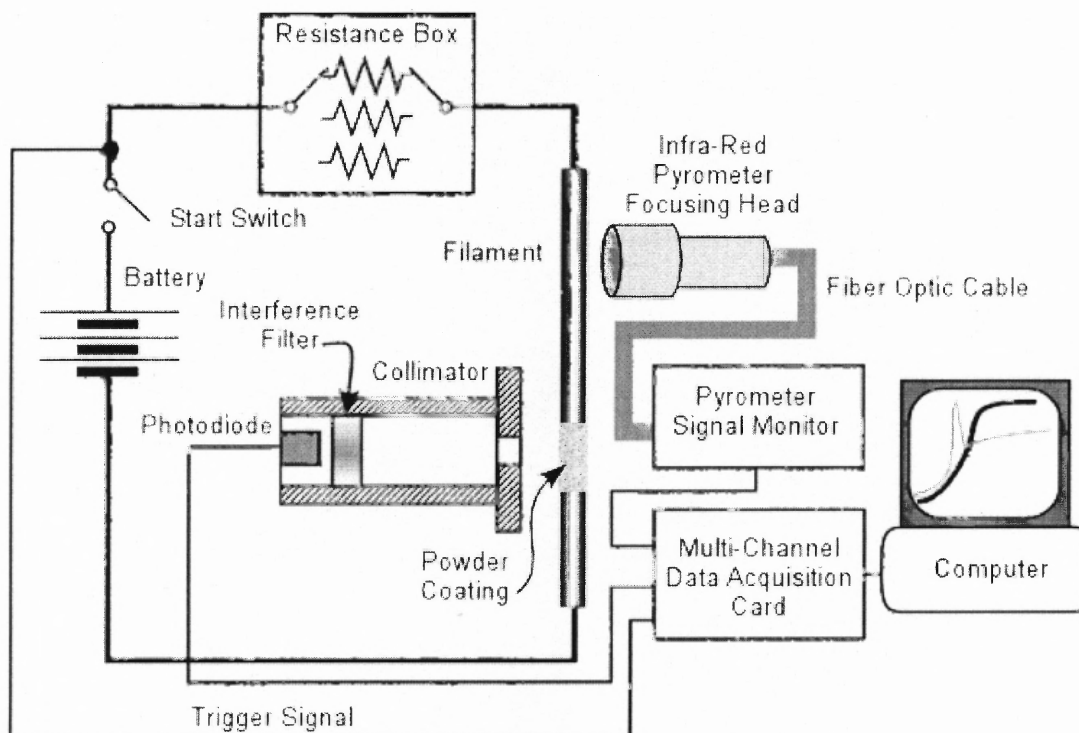
Figure 2.3 Schematic of the heated filament ignition setup.

The Nickel-Chromium filament is type Chromel-C resistance wire with a composition of 59.2% Nickel, 23.5% Iron, 16% Chromium and 1.3% Silicone. It is a nominally 24 gauge wire (510.5 μm) from ARCOR Electronics [15]. The wire from the spool is manually strain hardened (stretched) before each experiment in order to straighten before mounting in the electrodes. The actual wire diameter was measured to be 492 μm from an SEM image of the filament. Similarly, the coating thickness was

measured from the SEM images as shown in Figure 2.4. The wire has an electrical resistance of 5.482 Ω/m [15]. To compensate for the thermal expansion during heating, one electrode is attached to a linear slide with a tensioning spring. The filament length is set before each run to 4.67 cm using a gauge block.

2.3.1 Powder Coating Technique and Effective Coating Thickness

The coating on the filament is applied using a slurry of the Mg powder and hexane. Hexane was chosen as the solvent because it will not promote Mg oxidation unlike water. The slurry was applied to the center of the filament using a small paintbrush. A template with a 9.5 mm cutout was used to maintain a reproducible coating length. The coating was allowed to dry completely before the experiment.

To determine the thickness of the produced coating, SEM images of the coated samples were analyzed. A coated filament was prepared exactly as for the ignition experiment and placed on the SEM sample holder. Figure 2.4 is a SEM image of the coated filament cantilevered off the side of the SEM sample holder. The coating thickness changes along the filament: its edge on the right is very thin, it ramps up to a constant thickness until the cantilevered end, where a hump is observed. These thin regions and humps are also observed in the experiment, so this image is characteristic of the experimental imperfections. Figure 2.4 shows that the diameter of the coated filament in the region of the constant coating thickness is 602.9 μm, which corresponds to a coating thickness of 56 μm. The same coating thickness was determined from several similar images. Thus, the nominal number of layers of powder on the filament is six, considering the volumetric mean particle diameter of 9.7 μm (see Figure 2.1).
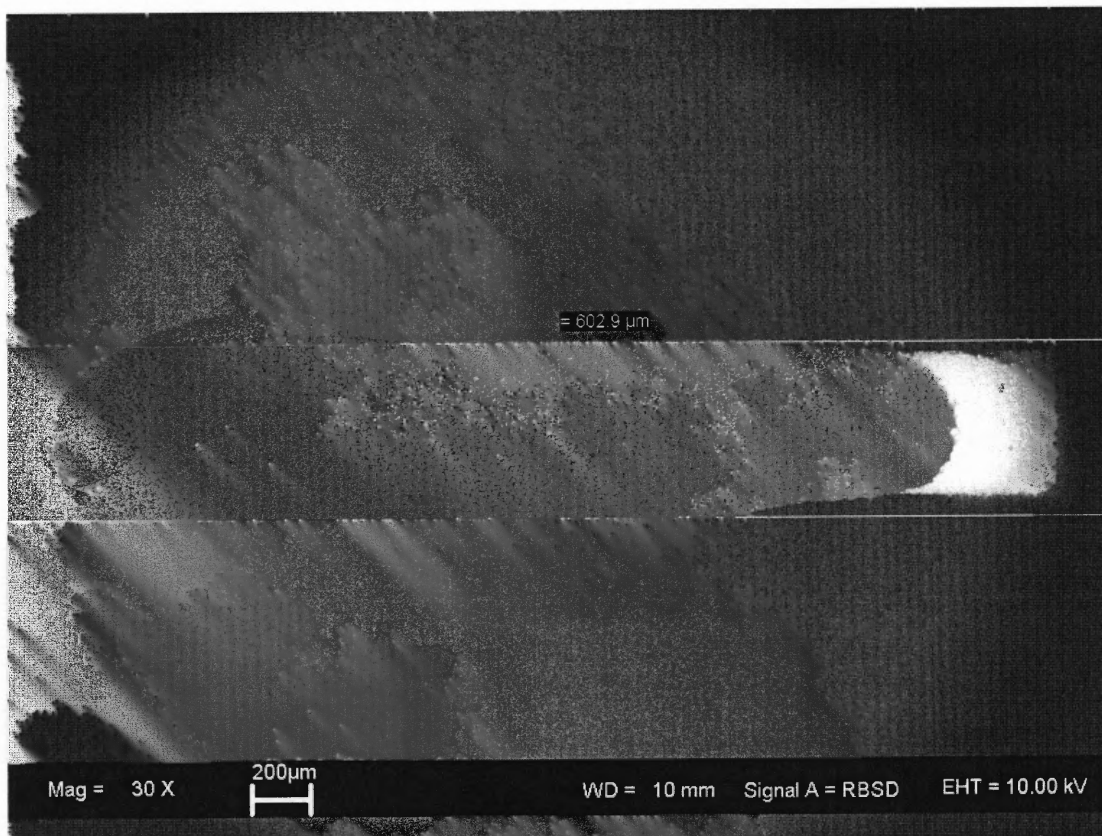
Figure 2.4 SEM image of the coated filament.

2.3.2 Pyrometer Calibration and Focusing

The pyrometer was calibrated using a Blackbody Calibrator (BB-4A) from Omega Engineering, Corp. in a temperature range between 800K and 1200K. The pyrometer sensor was placed so that its field of view was on the central, constant temperature surface of the emitter, not the side walls where a large temperature gradient exists. The emissivity setting on the pyrometer monitor was adjusted to 0.99 as given by the calibration unit. Three calibration readings for each 20K increment were taken by the data acquisition system.

The voltage versus temperature data from the calibration are shown in Figure 2.5. The calibration trend was linear and the measurements at each temperature were reproducible. The linear calibration equation for the pyrometer is:

$$T = 573.1 \cdot V + 247.8 \tag{2.1}$$

where T is the temperature in Kelvin and V is the measured voltage in Volt.
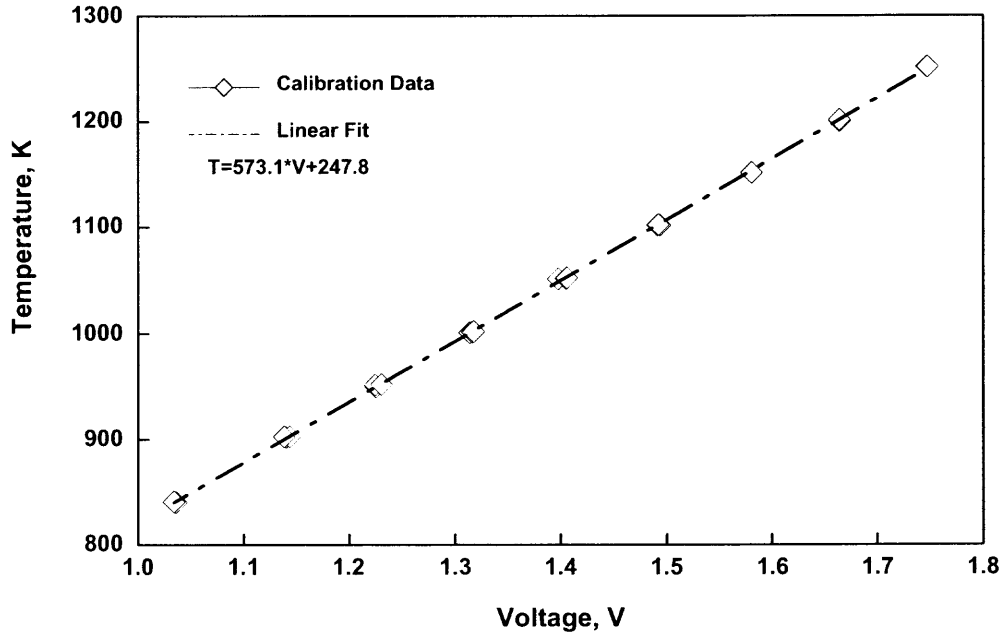
Figure 2.5 Pyrometer calibration plot and linear fit of experimental data.

For every ignition experiment, the pyrometer had to be focused so that the focal point was on the filament surface. Using a light source and a fiber optics guide, the light beam was directed through the pyrometer optics onto the filament, and focused two millimeters away from the edge of the powder coating. The distance of the lens from the filament was adjusted such that the focal point of the beam was on the surface of the filament. The emissivity of the Nickel-Chromium wire was taken to be 0.75 after consulting several sources [16-19].

2.3.3 Heating Rate Control

Five heating rates were used to experimentally determine the ignition kinetics of the Mg

powder. The heating rate was controlled by adjusting the external resistance and the DC

voltage in the electrical circuit shown in Figure 2.3. The lower four heating rates

correspond to a single battery voltage of 12V and external resistances of 1988, 1404, 638,

and 134 mΩ, respectively; where the resistances were measured using a milliohm meter,

model 380460 from EXTECH Instruments, Inc. The highest heating rate corresponds to

a 24V supply voltage using two batteries in series, and an external resistance of 134 mΩ.

These resistances do not include the internal resistance of the batteries.

For each heating rate, ten to eleven experiments were performed. A clean

filament was used for each repetition and the slurry was changed every 4-5 experiments.

2.4 Data Processing

The voltage signals acquired from the pyrometer and photo detector in the experiments

were processed using a MATLAB routine, which is given in Appendix B. In the case of

the four lower heating rates, the ignition instant was readily identifiable by a sharp

increase in the photodiode signal as the Mg began burning. For the highest heating rate,

the ignition instant is not as sharp, thus a consistent procedure for identification of the

ignition instant was necessary. Examples of the experimental traces for the pyrometer

and photodiode are given in Figure 2.6 and Figure 2.7 for the low and high heating rates.

Two approaches were implemented to find the ignition instant for the respective heating

rates.

As noted above, the lower four heating rates all had sharp increases in the photodiode signal that were interpreted as the ignition instant. The experimental traces in Figure 2.6 correlate to the second lowest heating rate of 317 K/s. For this heating rate, the photodiode signal indicates two peaks in the radiation signature after a steady increase due to the filament grey body radiation; the first peak is approximately 50 ms before the second as shown in Figure 2.6. This first peak is associated with a group a particles that ignite before the entire coating. The onset of the first peak is thereby taken to be the ignition instant, which is indicated on the figure as the vertical dashed line. The ignition temperature is the measured pyrometer temperature at the ignition instant and the heating rate is computed as the slope of the pyrometer temperature over a temperature interval of 20 K, immediately preceding the ignition.
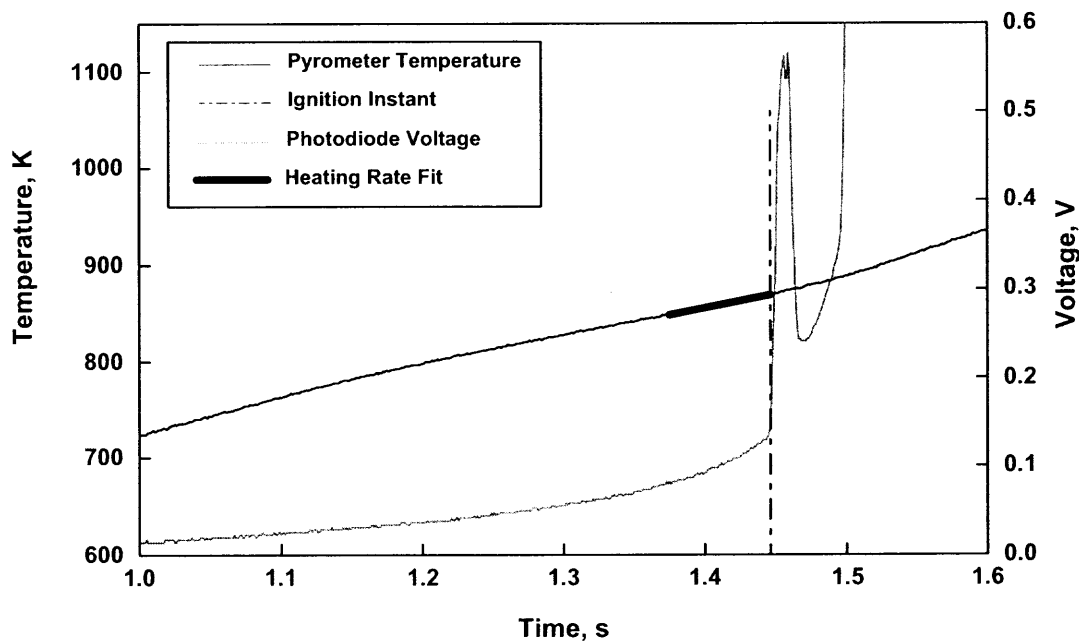
Figure 2.6 Experimental traces for pyrometer and photodiode at a low heating rate.

For the highest heating rate of 15,724 K/s, a different procedure was used for the data processing. Figure 2.7 illustrates the pyrometer temperature and photodiode signal for the highest heating rate near ignition. The ignition instant was determined by comparing two secant lines attached to the photodiode trace. Both secant lines spanned a time interval of 1.8 ms, and ignition was arbitrarily determined when the leading secant line had a slope three times that of the trailing secant line. The time span and slope ratio were both selected such that the ignition event occurred between two specific events. The first event would be the instant when the powder radiation signal diverges from the baseline radiation signal emitted by the filament without powder heated with the same voltage. The second event would be the time at the maximum derivative of the radiation signal. Typically, the filament temperature difference between these two events is 50 K. Therefore, the arbitrary selection of the ignition instant could introduce a 50 K bias error on the ignition temperature.
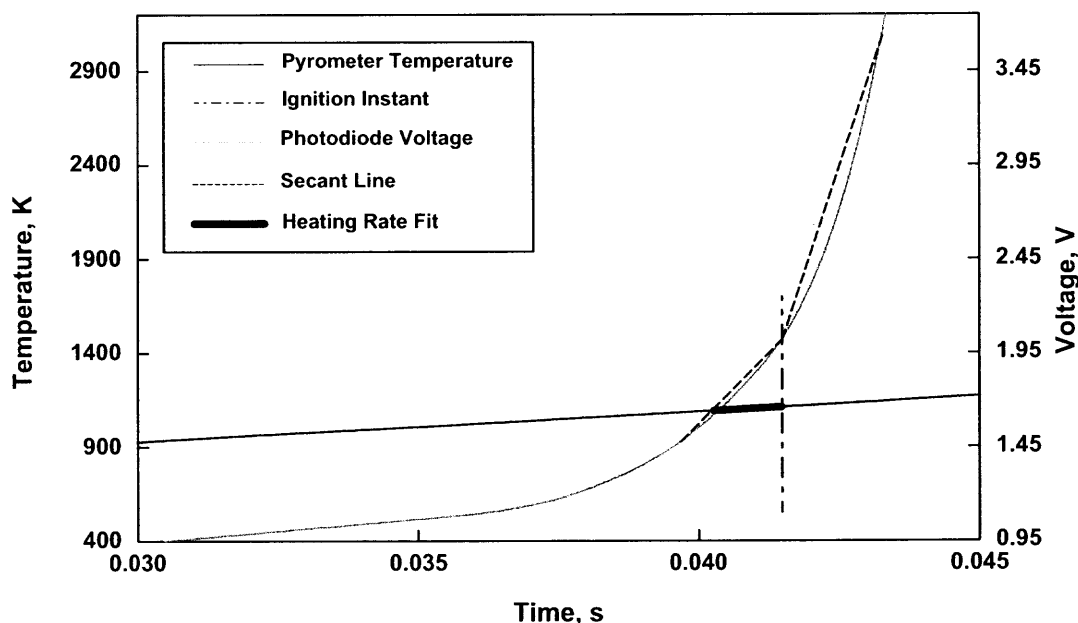
Figure 2.7 Experimental traces for pyrometer and photodiode at a high heating rate.

CHAPTER 3

LASER FLASH DIFFUSIVITY EXPERIMENT

3.1 General Description and Apparatus

The thermophysical properties of magnesium powder are needed to describe the heat transfer in the powder coating. If the bulk thermal diffusivity of the powder is known, then the thermal transport through the powder by conduction can be found. The thermal diffusivity, α, is related to the thermal conductivity, k, by the material density, ρ, and heat capacity, C, as:

$$\alpha = \frac{k}{\rho C} \tag{3.1}$$

A technique called the flash method was developed in 1960 by Parker, Butler, and Jenkins [11] where the thermal diffusivity of a small sample can be found. The technique is primarily used to measure the thermal diffusivity of thin metal disks by heating the face of the disk with a short burst of energy from a flash lamp or laser on the order of a millisecond or less. The resulting temperature rise at the rear surface can be measured and the thermal diffusivity is calculated from the temperature versus time data. Specifically, the time, $t_{1/2}$, when the temperature is at one half of its maximum value is found and the thermal diffusivity is computed using the empirical expression from Reference [11]:

$$\alpha = \frac{1.39L^2}{\pi^2 t_{1/2}} \tag{3.2}$$

where L is the depth of the sample.

The flash method was adapted for Mg powder by selecting a compatible sample geometry and experiment time scale since the powder is much less conductive than pure Mg. A schematic of the flash diffusivity technique employed for Mg powder is shown in Figure 3.1. The powder is loaded into a cylindrical cavity in a thermal insulator with a known depth L. The front face of the sample is heated with a 125W CO_2 laser, model Evolution 125 from SYNRAD, Inc., and the temperature at the rear face is measured with a thermocouple. This experiment was performed using three different samples and 5-6 trials per sample. The respective density of the samples was also determined by measuring the net powder mass and the cavity diameter and depth.
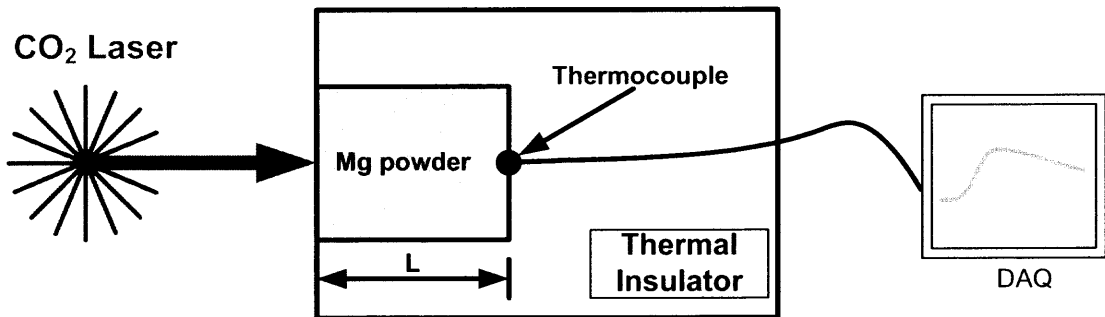
Figure 3.1 Schematic of the flash diffusivity experiment.

3.2 Procedure

3.2.1 Thermocouple Fabrication

A micro-thermocouple is made from nickel-chromium and constantan wires from OMEGA Engineering. The thermocouple has a maximum temperature range between - 200 and 900 °C and a generated electromotive force (EMF) over this temperature range of -9.835 to 76.373 mV. The thermocouple wires are twisted and tinned with solder; at

the first wire crossing, the wire is cut to form a small junction. One thermocouple was used for all experiments so the response time was effectively constant. Note that the thermocouple was not calibrated because the experiments cover only a narrow temperature range and the only parameter of interest was time, $t_{1/2}$.

3.2.2 Sample Preparation and Positioning

The thermally insulating holder shown in Figure 3.1 was made from an alumina-silica based ceramic fiber board. A hole is drilled in the face of the board with a #41 drill bit, 0.096 inches (2.44 mm), with a depth of 0.215 inches (5.5 mm). The thermocouple junction was placed through a pinhole at the rear surface, flush with the rear wall. The drilled cavity of the thermal insulator was treated with superglue to provide rigid walls and be less hygroscopic. Initial experiments with sample depths of 1, 2.5, and 5.5 mm were conducted and the sample depth of 5.5 mm was selected because of the best reproducibility of the measurements. The sample cavity is filled using a slurry of the Mg powder and hexane, similar to the ignition experiment, and packed lightly (not pressed). The surface of the sample was wiped clean with a brush and the sample was placed in a vacuum chamber to evaporate the remaining hexane.

A visible laser aligned with the CO_2 beam is used to identify the sample location to be heated. In order to correct for minor misalignment, before placing the sample in the laser testing chamber, a stock piece of heat insulator was used to visualize the CO_2 laser's beam. After the beam location was found, the sample was fixed to a sliding table and positioned so that the beam was focused at the center of the cavity. The laser beam itself was not centrally focused on the sample, but defocused such that a 5 mm diameter area was heated directly.

3.2.3 Laser and Data Acquisition Parameters

Several issues were addressed when selecting the laser operating parameters such as power and pulse duration. The laser power had to be high enough to acquire a strong signal from the thermocouple, but low enough to not melt or ignite the Mg powder on the sample face. Similarly, the laser pulse duration had to be long enough to achieve a strong signal, but short enough not to interfere with the sample equilibration time. Based on initial experiments, the operating parameters were a laser power of 3.5 % and a pulse duration of 5 s.

The data acquisition system used to generate the laser trigger and record the thermocouple voltage is a National Instruments BNC-2110 multi-channel board and PCI-MIO-16E-4 card. The thermocouple signal is sampled at a rate of 500 s^{-1} for 40 s.

3.3 Data Processing

A typical temperature (voltage) profile for the rear surface of the sample as measured by the thermocouple is shown in Figure 3.2. The signal is very noisy because the EMF generated by the thermocouple is very close to the minimum resolution for the BNC-2110 data acquisition board. This thermocouple signal is the best acquired given the constraints on laser power and duration. During the initial laser pulse of 5 s there is no temperature increase at the rear surface, between 8 and 30 s the sample temperature equilibrates, and the maximum temperature is achieved after 30 s. In order to better determine the half time, the experimental data were smoothed using a locally weighted linear regression "lowess" method available in MATLAB.
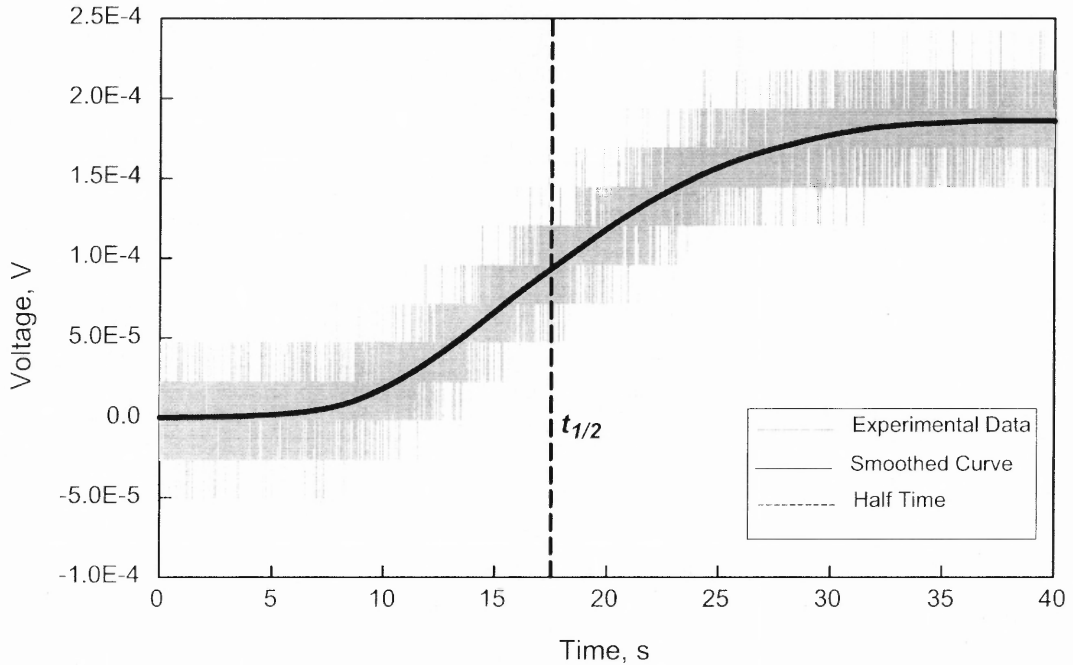
Figure 3.2 Sample voltage trace acquired from thermocouple for flash diffusivity experiment and corresponding smoothed curve.

The locally weighted linear regression is used to smooth data, where each smoothed value is determined by neighboring data points defined within the span. The process is weighted because a regression weight function is defined for the data points contained within the span. The local regression smoothing process follows these steps for each data point: 1) compute the regression weights for each data point in the span using the tricube function:

$$\omega_i = \left(1 - \left| \frac{x - x_i}{d(x)} \right|^3 \right)^3 \tag{3.3}$$

where x is the predictor value associated with the response value to be smoothed, x_i are the nearest neighbors of x as defined by the span, and $d(x)$ is the distance along the abscissa from x to the most distant predictor value within the span. The data point to be

smoothed has the largest weight and the most influence on the fit, and data points outside the span have zero weight and no influence on the fit. 2) Perform a weighted linear least squares regression using a first degree polynomial. 3) Calculate the smoothed value at the predictor value of interest given by the weighted regression.

The smoothed line (solid bold) shown in Figure 3.2 is calculated using a span of 10% of the total number of data points. Using the smoothed line, $t_{1/2}$ is computed as the time when the temperature is half the maximum value, which is 17.5 s for this experiment and is illustrated by the dashed vertical line in Figure 3.2. The MATLAB source code can be found in Appendix B for the program used to smooth the data and find the half time.

CHAPTER 4

HEAT TRANSFER MODEL

4.1 Approach

Modeling the heated filament ignition experiment requires one to address several issues. It is necessary to theoretically characterize the powder coating on the filament and determine the contact resistance between particles. It is also necessary to formulate the energy balance for the filament and powder layers using the explicit finite difference method. The energy balance for the powder layer will involve a term to represent the chemical heat generated by the oxidation reaction. Lastly, the particle temperatures will be found numerically using an adaptive time step and the ignition instant will be found by specifying an ignition criterion. The associated ignition temperature at the ignition instant will be the calculated filament temperature at the same location where the pyrometer is focused in the experiments.

4.2 Coating Properties

4.2.1 Coating Geometry and Packing

To model the powder coating on the filament, a packing structure must be assumed. One critical simplifying assumption was made in defining the packing structure, which is that the Mg powder is a homogeneous monodispersed powder with particle diameters equal to that of the volumetric mean diameter determined from the size analysis. The second assumption is that the coating has a hexagonal close packed structure (HCP) with a

theoretical packing density of 74%. Given these assumptions, the thermal properties of the coating, which are assumed to be similar to those of the flash diffusivity sample, can be derived.

The powder coating on the filament is illustrated in Figure 4.1A for the case of N layers, where the particle diameter is d_p. From the HCP structure, a particle in each layer has three contacts with the neighboring particles above and below as illustrated in Figure 4.1B. Note that the first layer of particles will only have one contact with the filament. The distance between layers is the height of the tetrahedron formed by the particle centers, shown as H in Figure 4.1B. These geometric properties will be used to derive the contact resistance between particles using the bulk thermal diffusivity and bulk density measured in the flash diffusivity experiment.

(A)   (B)
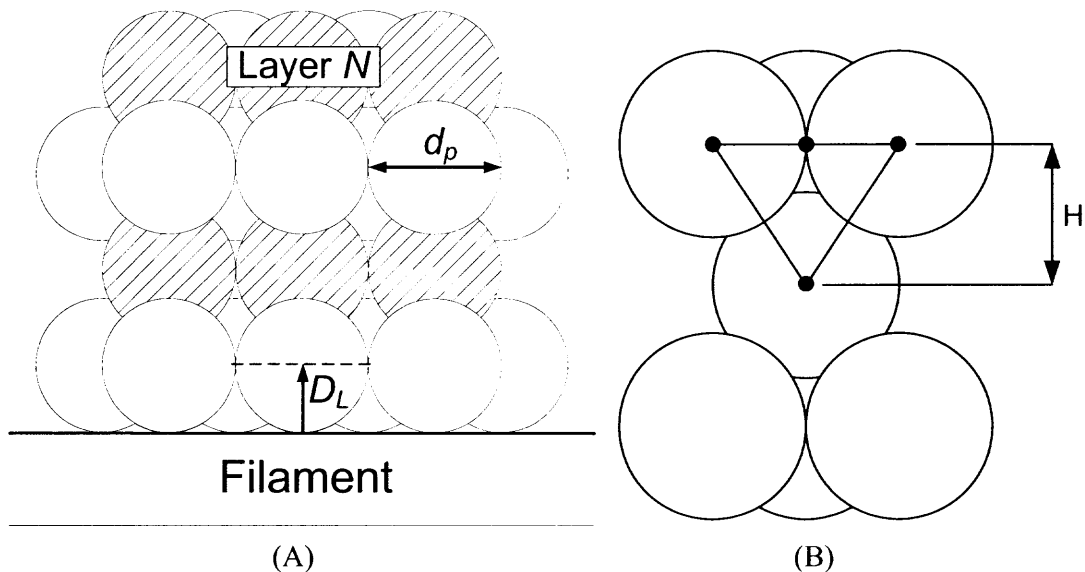
Figure 4.1 (A) illustration of layers in coating sitting on the filament, (B) illustration of particle contacts and height between layers.

4.2.2 Contact Resistance Formulation

The contact resistance between individual particles is needed to describe the conduction through particle layers in the heat transfer model of the coating. The contact resistance will be derived for a bulk control volume of Mg powder using the measured thermophysical properties. The hexagonal close packed structure in the control volume can be thought of as multiple planar particle-layers stacked in the arrangement illustrated in Figure 4.1. However, the actual packing is likely to be imperfect resulting in a lower average density and reduced average number of contacts for a single particle. The actual number of particle contacts, η, can be estimated using the volumetric ratio of the measured bulk density, ρ_b, to the theoretical packing density, ρ_{HCP}:

$$\eta = 3\frac{\rho_b}{\rho_{HCP}} \tag{4.1}$$

Considering that the filament diameter is much greater than the coating thickness, the derivation for the individual contact resistance between particles was obtained through analysis of a bulk thermal resistance, R_b, for the planar control volume:

$$R_b = \frac{l}{k_b A} \tag{4.2}$$

where k_b is the bulk thermal conductivity, l is the thickness of the control volume in the direction of heat transfer, and A is the cross sectional area of the control volume in the direction normal to that of heat transfer. For the control volume filled with powder, the thickness will be determined as the product of the number of layers, N, and the distance between the layers, H. H is defined for the HCP structure as:

$$H = \sqrt{\frac{2}{3}}d_p \tag{4.3}$$

Thus, l can be expressed as:

$$l = \sqrt{\frac{2}{3}} N d_p \tag{4.4}$$

From Equation (3.1), the thermal conductivity, k_b, can be expressed through the bulk thermal diffusivity, α_b, bulk density, ρ_b, and specific heat, C_b. Substituting Equations (4.4) and (3.1) into Equation (4.2), the bulk resistance becomes:

$$R_b = \frac{N\sqrt{2/3}d_p}{\alpha_b \rho_b C_b A} \tag{4.5}$$

The resistance of a single particle layer, R_{layer}, in the planar control volume is related to the bulk resistance through the number of layers by:

$$R_{layer} = \frac{R_b}{N} \tag{4.6}$$

The total resistance of a particle layer can be defined as a parallel arrangement of resistances for all individual particle contacts. Thus, the layer resistance is related to the individual contact resistance, $R_{contact}$, by:

$$\frac{1}{R_{layer}} = \frac{\eta \, n_{layer}}{R_{contact}} \tag{4.7}$$

where n_{layer} is the number of particles in the layer. The number of particles in each layer is determined using the ratio of layer cross section area to the effective particle cross section area corrected considering the difference in the measured and theoretical packing densities (see Equation (4.1)). For the HCP model, the number of particles in a layer is:

$$n_{layer} = \frac{A}{d_p^2} \frac{\rho_b}{\rho_{HCP}} \tag{4.8}$$

The layer resistance can be rewritten by substituting Equation (4.8) into Equation (4.7) and rearranging as:

$$R_{layer} = \frac{R_{contact} d_p^2 \rho_{HCP}}{\eta A \rho_b} \qquad (4.9)$$

From the relationship between the layer resistance and bulk resistance given in Equation (4.6), and from the definition of the layer resistance and bulk resistance by Equations (4.9) and (4.5), the contact resistance for the individual particle contact is expressed as:

$$R_{contact} = \frac{\rho_b}{\rho_{HCP}^2} \frac{\sqrt{6}}{d_p \alpha_b C_b} \qquad (4.10)$$

Equation (4.10) is the contact resistance expression that describes the conduction through the particle layer. It is a function of the bulk thermal diffusivity, bulk density, and volumetric mean particle diameter, which are all measured properties of the Mg powder used.

4.2.3 Particle Layer Geometry Corrections

Since the thermal contact resistance was based on a planar control volume, additional assumptions and corrections will be made to account for packing differences between the cylindrical coating geometry and the planar geometry. The distance between layers is assumed to be unaffected by the growing number of particles in each concentric layer as the radial distance from the filament increases. However, a correction should be introduced for the number of contacts between the layers due to a greater number of particles in the outward layers. The correction factor is the ratio between the numbers of particles in the contacting layers.

The number of particles in each coating layer, $n_{coating\ layer}$, is determined by the ratio between the cylindrical surface area of the layer and the effective particle cross section area, and is corrected by the measured bulk density:

$$n_{coating\ layer} = \frac{\pi D_L L_c}{d_p^2} \frac{\rho_b}{\rho_{HCP}}$$
(4.11)

where D_L is the diameter of the layer, and L_c is the coated distance along the filament. The diameter of any layer, n, in the filament powder coating for the HCP structure can be expressed as:

$$D_L(n) = D_f + d_p \left[1 + \sqrt{\frac{8}{3}}(n-1) \right]$$
(4.12)

where D_f is the filament diameter.

Considering Equations (4.11) and (4.12), the correction factor for the number of contacts in each layer is simply reduced to the ratio of the layer diameters.

4.3 Filament Modeling

The filament was modeled as a horizontal cylinder clamped at both ends to a large constant temperature plate. The filament was one dimensionally meshed and the energy balance equations were formulated using explicit finite difference method. A heat generation term is required in the energy balance because the filament is electrically heated. Additionally, the losses to the powder were accounted for at the respective powder location.

4.3.1 Discretization and Boundary Conditions

The filament is treated one dimensionally because the conduction within the filament is much greater than the surface convection; thus, the internal filament temperature is lumped and the temperature gradient in the radial direction is neglected. The filament was discretized using a finite difference nodal network and is illustrated in Figure 4.2 with M as the total number of nodes. The network has constant temperature boundary conditions fixed at room temperature, 298 K. The nodal spacing is Δx and the intermediate elements are labeled m. All nodes are subject to the surrounding environment, except for those coated with powder where the losses are only to the coating.
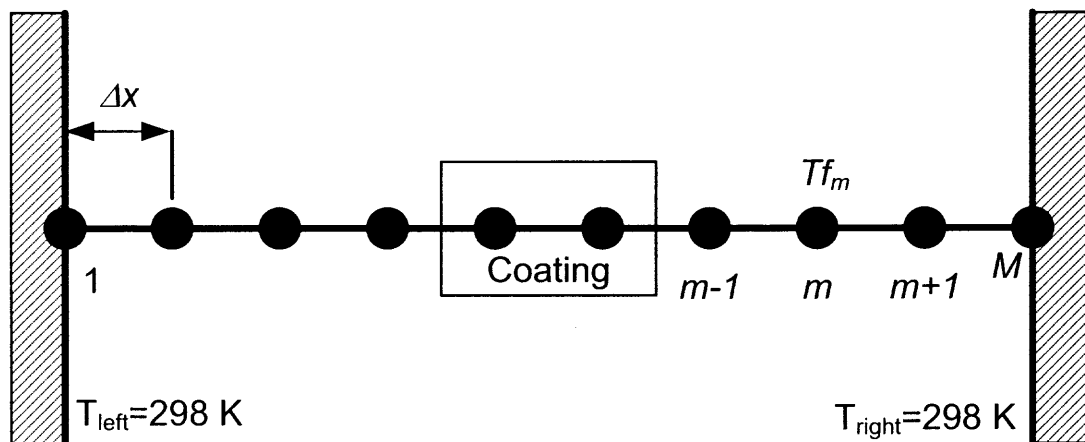
Figure 4.2 Nodal network for filament.

4.3.2 Filament Energy Balance

The energy balance for an element m in the nodal network for the filament can be written in terms of the heat conduction, convection, radiation, losses to the powder, and heat generation as:

$$\dot{Q}_{conduction} + \dot{Q}_{radiation} + \dot{Q}_{convection} + \dot{Q}_{powder} + \dot{G}_{element} = \Delta\dot{E}_{element} \qquad (4.13)$$

where $\dot{Q}_{conduction}$ is the conductive heat transfer, $\dot{Q}_{radiation}$ is the radiation heat transfer, $\dot{Q}_{convection}$ is the convective heat transfer, $\dot{Q}_{powder}$ is the heat losses to the powder, $\dot{G}_{element}$ is the heat generated in the element, and $\Delta\dot{E}_{element}$ is the change in internal energy of the control volume. The conductive loss to the powder, $\dot{Q}_{powder}$, will only apply to the powder nodes and at these nodes the convection loss to the environment is neglected. Each heat transfer mechanism will be outlined in the following.

The one dimensional conduction for node m is formulated using the Fourier equation with a constant thermal conductivity k_f for the Nichrome filament:

$$\dot{Q}_{conduction} = k_f \frac{\pi\left(D_f\right)^2}{4} \frac{dTf_m}{dx} \qquad (4.14)$$

where Tf_m is the temperature of element m and the cross section area is given for the filament diameter, D_f.

The radiation loss to the environment at temperature T_∞ for all elements of the uncoated filament surface is expressed as:

$$\dot{Q}_{radiation} = \varepsilon\sigma\pi D_f \Delta x\left(\left(T_\infty\right)^4 - \left(Tf_m\right)^4\right) \qquad (4.15)$$

where ε is the emissivity of the Nichrome filament, and σ is the Stehan-Boltzmann constant. The emissivity of the Nichrome filament was taken to be 0.75 [16-19]. For the

elements in contact with the powder where the radiation loss is only to the powder, the environment temperature, T_∞, is replaced with the particle temperature of the first powder layer, $T_{p,1}$, in Equation (4.15).

Natural convection on the filament surface was the only mode of convection because the filament and electrodes are mounted in a closed chamber. Therefore, the Nusselt number (dimensionless heat transfer coefficient) for natural convection around a horizontal cylinder was determined. The properties of air, such as kinematic viscosity, thermal conductivity, and Prandtl number were found at the film temperature, T_{film}, defined by:

$$T_{film} = \left(\frac{Tf_m + T_\infty}{2} \right) \tag{4.16}$$

The Rayleigh number, Ra, a dimensionless quantity that represents the flow regime of the fluid and depends on the buoyancy and viscous forces, is found using the air properties at T_{film} [20]:

$$Ra = \frac{g \left(\dfrac{1}{T_{film}} \right) \left(Tf_m - T_\infty \right) D_f^3}{\left(v\left(T_{film} \right) \right)^2} \left(\Pr\left(T_{film} \right) \right) \tag{4.17}$$

where g is the gravitational constant, v is the kinematic viscosity at T_{film}, and Pr is the Prandtl number at T_{film}. Finally, the average Nusselt number, Nu_f, for the natural convection around the filament can be obtained [20]:

$$Nu_f = \left[0.6 + \frac{0.387 \left(Ra \right)^{1/6}}{\left[1 + \dfrac{0.559}{\Pr\left(T_{film} \right)^{9/16}} \right]^{8/27}} \right]^2 \tag{4.18}$$

Thus, the convective heat transfer, $\dot{Q}_{convection}$, from the filament element is:

$$\dot{Q}_{convection} = Nu_f k_{air}\left(T_{film}\right)\pi\Delta x\left(T_\infty - Tf_m\right) \tag{4.19}$$

where $k_{air}(T_{film})$ is the thermal conductivity of air evaluated at the film temperature.

The losses to the powder coating, $\dot{Q}_{powder}$, for the element in contact with the coating are conductive losses due to the contact resistance between the filament and the first layer of particles. The contact resistance with the filament is assumed to be similar to the contact resistance between particles as determined in Equation (4.10). The losses to the powder can then be described using $R_{contact}$ and the total number of contacts between the filament and particles per filament element:

$$\dot{Q}_{powder} = \frac{\pi\Delta x D_{L,1}}{d_p^2}\frac{T_{p,1} - Tf_m}{R_{contact}} \tag{4.20}$$

where $D_{L,1}$ is the diameter of the first layer of powder, and $T_{p,1}$ is the temperature of the first layer of powder.

The heat generated in the filament is from the Nichrome's resistance to the passing electric current. An equivalent electric circuit model is illustrated in Figure 4.3. The external resistance, R_{ext}, is from the resistance switching box and other miscellaneous resistances in the network including the unknown internal resistance of the battery. The external resistances are treated as an adjustable parameter in order to fit the filament temperature profile with experimental temperature profiles for the various heating rates. The filament resistance, R_f, can be estimated using the resistivity, ξ, of the Nichrome filament as:

$$R_f = \frac{4\xi\Delta x}{\pi D_f^2} \tag{4.21}$$
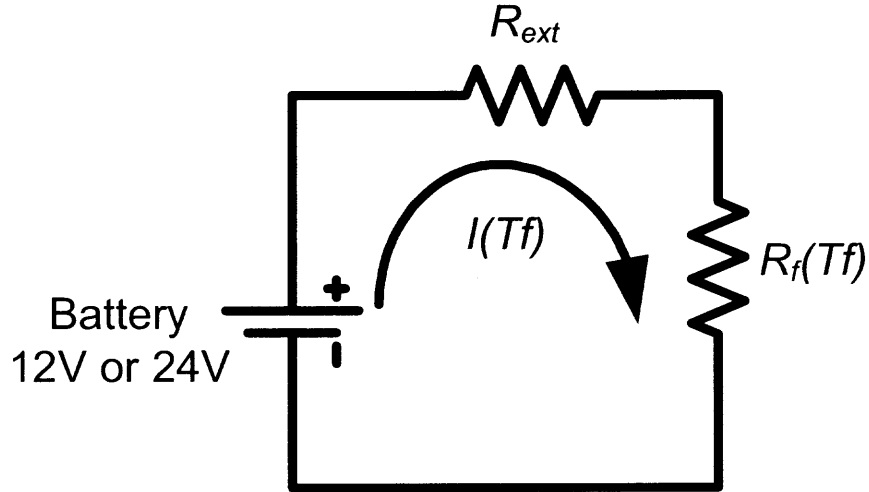
Figure 4.3 Electrical circuit used to model the filament heating.

The current in the circuit shown in Figure 4.3 is found using Ohm's law. To account for the temperature affected resistance changes of the Nichrome filament, a temperature dependent resistance coefficient, $C_{resistance}$, has been introduced from the literature [21,22]. The resistance coefficient for the Nichrome filament is given in Figure A.1 in Appendix A for a selected range of temperature. For temperatures outside the reference values, the resistance coefficient was extrapolated. Thus, the current, I, as a function of filament temperature is expressed as:

$$I(Tf) = \frac{V}{R_{ext} + C_{resistance}(Tf)R_f}$$ (4.22)

The heat generated for an element in the filament can then be expressed as a function of the current and filament resistance as:

$$\dot{G}_{element} = (I(Tf))^2 C_{Resistance}(Tf)R_f$$ (4.23)

The change in energy of the filament element, $\Delta \dot{E}_{element}$, as a function of the Nichrome properties and time rate of change for the element temperature is:

$$\Delta \dot{E}_{element} = \rho_f V_f C_{p,f} (Tf) \frac{dTf_m}{dt} \tag{4.24}$$

where ρ_f is the filament density, V_f is the filament volume, and $C_{p,f}(Tf)$ is the temperature dependent specific heat. The specific heat of the Nichrome filament was calculated using MTDATA software, available for download from the National Physical Laboratory [23]. The calculated specific heat is given in Figure A.2 in Appendix A for the solid phase temperature range.

Substituting the above equations into the energy balance in Equation (4.13), the filament temperature Tf_m for element m is obtained by numerically integrating Equation (4.13) using the explicit finite difference method. The explicit method implies that the temperature is calculated at the next time step $i+1$ using the initial conditions from step i. The time step used to integrate over will be discussed below because it is dependent on the particle time step used in the coating heat transfer model which is calculated using an adaptive method, as is explained in Section 4.6.

4.4 Particle Temperature Modeling

The heat transfer modeling of the powder coating implements the packing structure and geometry that was assumed in the previous sections. Additional simplifying assumptions are used when deriving the energy balance equations for the powder coating. The first assumption is that the powder particle temperature is lumped so that no temperature gradient exists within the particle. This assumption is valid because the thermal resistance of metal is negligible when compared to the contact resistance between particles.

Therefore, the conduction heat transfer term is a sole function of the contact resistance. The second assumption is that the heat flow is only radial to the filament axis, which is consistent with the one dimensional heat flow assumed in the contact resistance derivation. Thus, all the particles in one layer have the same temperature. Convection within the gas trapped between the particles of the coating and at the coating sides is neglected, only the outermost layer experiences convective losses to the surrounding.

The powder coating is discretized one dimensionally using a finite difference nodal network illustrated in Figure 4.4. The network considers N total layers with intermediate layers labeled n. The boundary conditions for the network are the time dependent filament temperature at node 0, and convection and radiation losses to the environment at node N. The energy balance for each layer will be derived separately based on its interaction with the neighboring heat fluxes.
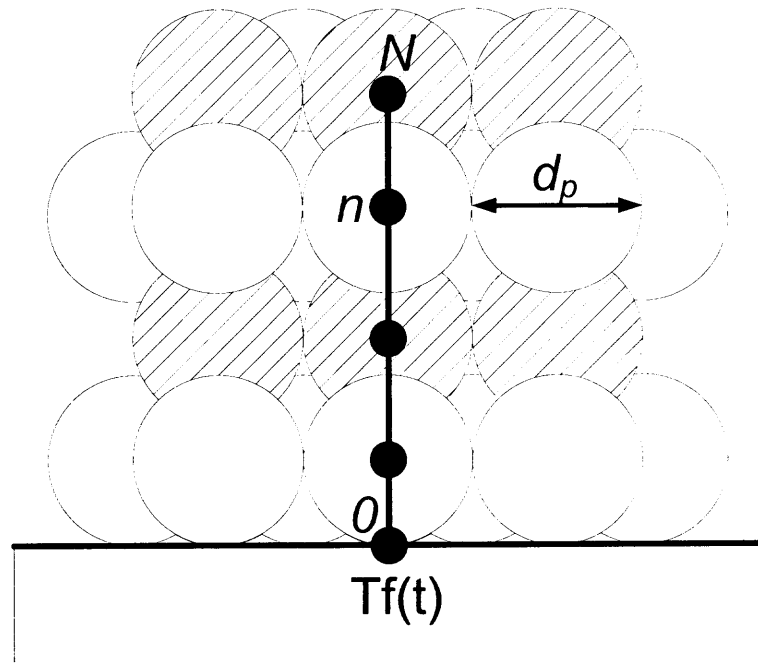
Figure 4.4 Nodal network for the powder coating.

4.4.1 Powder Electrical Conductivity

Since a large current is passing through the filament, the electrical properties of the

powder were tested to see whether heat generation would occur in the particles. A simple

experiment was used to test the electrical resistance of the powder. Figure 4.5 shows a

schematic of the experiment used to measure the electrical resistance. A channel was

milled in a polycarbonate block and copper electrodes were placed at each end of the

channel. The channel was packed with a slurry of Mg powder and hexane, and after the

hexane evaporated, the resistance was measured between both electrodes using a

milliohm meter. The resistance exceeded the maximum magnitude of the meter

indicating a very large electrical resistance. Therefore, the effect of the coating on the

filament resistance and the heat generation in the powder coating can be neglected.
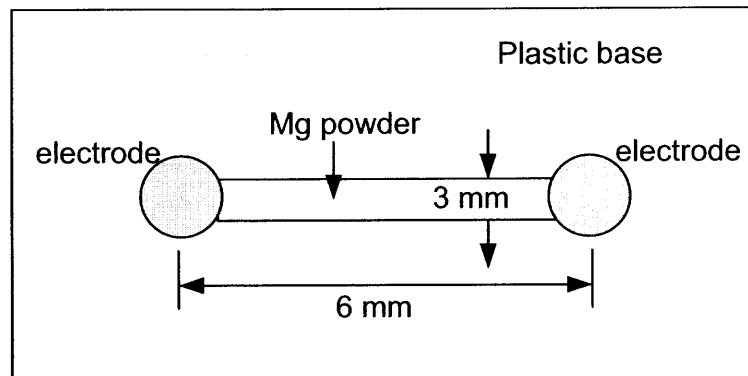
Figure 4.5 Schematic of the Mg powder electrical resistance experiment.

4.4.2 Particle Layer Contacting Filament

The powder layer in contact with the filament ($n=1$) has particles with only one contact

with the filament and three contacts with the above layer ($n=2$). The contact is assumed

to be similar to the contact between particles, which prevents introducing an unknown

parameter for this contact resistance. The energy balance for particle in the layer *n=1* can be written in terms of conduction, radiation, and chemical heat transfer as:

$$\dot{Q}_{conduction} + \dot{Q}_{radiation} + \dot{Q}_{chemical} = \Delta \dot{E}_p \qquad (4.25)$$

where $\dot{Q}_{conduction}$ and $\dot{Q}_{radiation}$ is the respective conduction and radiation between the filament and the neighboring particle layer, $\dot{Q}_{chemical}$ is the heat release due to all the thermo-chemical processes leading to ignition, and $\Delta \dot{E}_p$ is the change in internal energy of the particle.

The corrected number of contacts, η, is used for the contacts between layers. The conduction heat transfer, $\dot{Q}_{conduction}$, equation can be written out as:

$$\dot{Q}_{conduction} = \frac{\left(Tf_{M/2} - T_n\right) + \eta\left(T_{n+1} - T_n\right)}{R_{contact}} \qquad (4.26)$$

where $Tf_{M/2}$ is the filament temperature at the center node of the filament mesh, T_n is the temperature of the layer n, and T_{n+1} is the temperature of the neighboring layer above layer n.

The radiation term accounts for the heat transfer from the filament and the above particle layer. The effective surface area of the particle is its total surface area minus the contact area, where the contact area is an adjustable parameter. The emissivity of the particle, ε, and the filament is assumed to be the same with a value of 0.75. A view factor is introduced to correct for the actual area in view by the surroundings. The view factor, F, assumes that half the surface of the particle is in the field of view of the filament and the other half is in the field of view of the next layer of particles. The radiation heat transfer, $\dot{Q}_{radiation}$, is then:

$$\dot{Q}_{radiation} = \varepsilon\, \sigma F \left(A_{surface} - A_{contact} \right) \left[\left(Tf_{M/2} \right)^4 + \left(T_{n+1} \right)^4 - 2 \left(T_n \right)^4 \right] \tag{4.27}$$

where $A_{surface}$ is the total surface area of the particle, and $A_{contact}$ is the contact area correction.

To introduce the heat release from the thermo-chemical processes leading to ignition of the powder or other energetic material, a chemical heat transfer term, $\dot{Q}_{chemical}$, has been proposed, which is described similarly for all particles in the coating. The chemical term describes all processes such as surface oxidation, evaporation, and or vapor phase reaction that may generate heat in the particle. The rate of this chemical reaction is hypothesized to have Arrhenius type kinetics with a known activation energy E_A. The activation energy appropriate for description of ignition of magnesium powder, E_A=215 kJ/mol, was determined earlier in the literature [4,24-28] and confirmed using thermal analysis in Reference [10]. The pre-exponent, Z, is usually treated as an empirical adjustable parameter. The chemical term assumes that all particles in the coating have unlimited amount of oxygen to sustain the reaction and a single exponential function describes the reaction kinetics:

$$\dot{Q}_{chemical} = A_{surface} Z \Delta H \exp\left(-\frac{E_A}{RT_n} \right) \tag{4.28}$$

where $A_{surface}$ is the total particle surface area, ΔH is the specific heat of the oxidation reaction, and R is the universal gas constant. The changes in the specific heat of reaction caused by melting of the metal were accounted for using reference values for solid and liquid Mg from Reference [29].

The change in energy for a single particle, $\Delta\dot{E}_{particle}$, as a function of the powder properties is:

$$\Delta\dot{E}_{particle} = \rho_p V_p C_p \frac{dT_n}{dt} \tag{4.29}$$

where ρ_p is the particle density, V_p is the particle volume based on the volumetric mean diameter, and C_p is the particle specific heat. The Mg particle specific heat was calculated as a function of temperature using data from Reference [29] and is given in Figure A.3 in Appendix A.

4.4.3 Intermediate Particle Layer

For all particles in layers that are not in contact with the filament or environment, the energy balance is identical. The particles in such layers have particle layers above and below. The energy balance for a particle in a layer n can be written in terms of conduction, radiation, and chemical heat transfer as:

$$\dot{Q}_{conduction} + \dot{Q}_{radiation} + \dot{Q}_{chemical} = \Delta\dot{E}_{particle} \tag{4.30}$$

The conduction term can be formulated as a function of the contact resistance between the upper and lower particle layers and the layer n. However, the number of contacts, η, must be corrected. As discussed in Section 4.2.3, the ratio between the layer diameters, D_L, will correct the number of contacts η for the neighboring layers. Thus, $\dot{Q}_{conduction}$ can be written as:

$$\dot{Q}_{conduction} = \frac{\eta}{R_{contact}}\left[\frac{D_{L,n-1}}{D_{L,n}}\left(T_{n-1}-T_n\right) + \frac{D_{L,n}}{D_{L,n+1}}\left(T_{n+1}-T_n\right)\right] \tag{4.31}$$

where $D_{L,n-1}$, $D_{L,n}$, and $D_{L,n+1}$ are the respective layer diameters for layers $n-1$, n, and $n+1$; and T_{n-1}, T_n, and T_{n+1} are the respective temperatures for layers $n-1$, n, and $n+1$.

The radiation for the particles in the intermediate area of the coating only considers heat transfer from the layers above and below. The emissivity and view factor are unchanged, thus $\dot{Q}_{radiation}$ is:

$$\dot{Q}_{radiation} = \varepsilon \sigma F \left(A_{surface} - A_{contact} \right) \left[\left(T_{n-1}^f \right)^4 + \left(T_{n+1}^f \right)^4 - 2 \left(T_n^f \right)^4 \right] \tag{4.32}$$

For the layer n, the terms of $\dot{Q}_{chemical}$ and $\Delta \dot{E}_{particle}$ are similar to those in Equations (4.28) and (4.29).

4.4.4 Particle Layer in Contact with Surrounding

The particle layer N is the outermost layer in the coating and it has losses to the environment from radiation and convection. This is the only particle layer where convection is considered, so the convection coefficient must be determined for the coating geometry and temperature. The energy balance can be written in terms of conduction, radiation, chemical, and convection heat transfer as:

$$\dot{Q}_{conduction} + \dot{Q}_{radiation} + \dot{Q}_{chemical} + \dot{Q}_{convection} = \Delta \dot{E}_{particle} \tag{4.33}$$

The conduction for a particle in the layer N is only from the layer below. The number of contacts is corrected, thus, $\dot{Q}_{conduction}$ can be written as:

$$\dot{Q}_{conduction} = \frac{\eta}{R_{contact}} \left[\frac{D_{L,N-1}}{D_{L,N}} \left(T_{N-1} - T_N \right) \right] \tag{4.34}$$

The radiation term now includes the heat transfer to the surrounding environment. The emissivity and view factor are unchanged, thus $\dot{Q}_{radiation}$ is:

$$\dot{Q}_{radiation} = \varepsilon \sigma A_{surface} F \left(\left(T_{n-1} \right)^4 + T_{\infty}^4 - 2 \left(T_n \right)^4 \right) \tag{4.35}$$

The convective heat transfer on the outer layer is determined using the Nusselt number calculated for a horizontal cylinder with the outer layer diameter. The film temperature, T_{film}, for the outer layer is defined by:

$$T_{film} = \left(\frac{T_N + T_{\infty}}{2} \right) \tag{4.36}$$

The Rayleigh number, Ra, is found using the air properties at T_{film} [20]:

$$Ra = \frac{g \left(\dfrac{1}{T_{film}} \right) \left(T_N - T_{\infty} \right) D_{L,N}^3}{\left(v \left(T_{film} \right) \right)^2} \left(\mathrm{Pr} \left(T_{film} \right) \right) \tag{4.37}$$

The average Nusselt number, Nu_p, for the natural convection around the coating can be obtained using Equation (4.18).

The average Nusselt number is valid for the entire coating surface, therefore, the convective heat transfer for the entire coating surface can be normalized to one particle using the total number of particles in layer N. Thus, the convective heat transfer, $\dot{Q}_{convection}$, from one particle in the outer layer is:

$$\dot{Q}_{convection} = \frac{Nu_p k_{air} \left(T_{film} \right) d_p^2 \rho_{HCP}}{D_{L,N} \rho_b} \left(T_{\infty} - T_N \right) \tag{4.38}$$

where $k_{air}(T_{film})$ is the thermal conductivity of air evaluated at the film temperature.

For layer N, the terms $\dot{Q}_{chemical}$ and $\Delta \dot{E}_{particle}$ are described, as discussed above by Equations (4.28) and (4.29), respectively.

4.5 Melting Consideration

Since the particle temperature is lumped, the particle melting is treated as an isothermal

process. When the particle temperature is equal to the melting point of the material, the

particle has a constant temperature until the heat required to completely melt the particle

is consumed. So when the particle temperature equals the melting temperature:

$$T_n \approx T_{melting} \tag{4.39}$$

The particle temperature remains constant until the particle has gained enough heat from

the surrounding sources to overcome the heat of fusion for the material, h_f, which can be

expressed in integral form as:

$$\int_{t_0}^{t} \dot{Q}_{input} dt \geq \rho_p V_p h_f \tag{4.40}$$

where t_0 is the start of melting, t is the current time, and $\dot{Q}_{input}$ is the heat supplied over

the time interval. After the melting condition in Equation (4.40) is satisfied, the particle

temperature is allowed to increase.

4.6 Time Step Selection

The time steps used to numerically integrate the energy equations for the filament and

powder layer were calculated using an adaptive method. Since the filament heating rate

varied between 90 K/s and 16,000 K/s, a constant time step for all heating rates would not

allow a stable and accurate solution unless it was extremely small, which is

computationally expensive. Additionally, the exponential expression, $\dot{Q}_{chemical}$, requires a

refined time step when the temperature starts increasing rapidly. Therefore, a systematic

approach was implemented to calculate the time step for all iterations based on linearly predicted temperature differences.

The adaptive approach considers the temperature history of the powder coating and fits a linear trendline such that the next time step is calculated for a constant temperature increase. The slope of the trendline is computed for the previous five time steps as illustrated in Figure 4.6. The temperature difference, ΔT_{step}, is an adjustable parameter. With a constant ΔT_{step}, the number of iterations and computation times for all heating rates are similar. The ΔT_{step} was determined to ensure that the ignition temperature of the coating converged to within 1 K. The ignition temperature convergence as a function of $1/\Delta T_{step}$ is shown in Figure 4.7, where $\Delta T_{ignition}$ is the difference between the ignition temperate for any ΔT_{step} and the smallest ΔT_{step}. Figure 4.7 indicates that the higher heating rates converge faster than the lower, and the corresponding ΔT_{step} for a 1 K convergence is 0.01 K. Upper and lower limits were assigned to the time step to avoid minor instabilities that could arise. Furthermore, the isothermal particle temperatures during melting requires the use of a fixed time step.
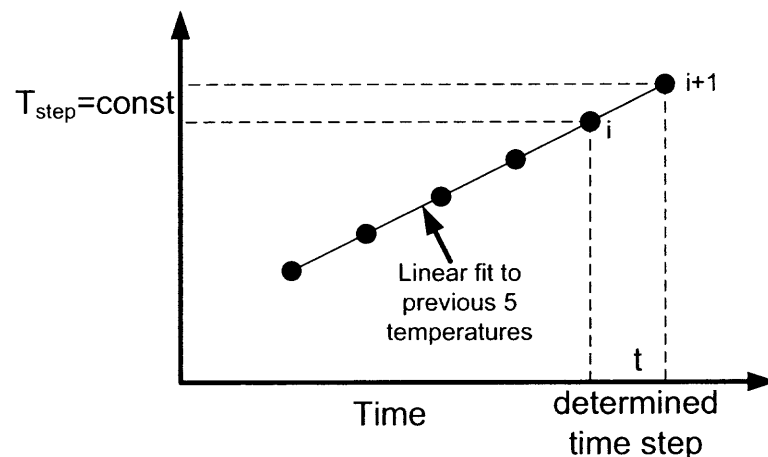
Figure 4.6 Time step calculation illustration.

The filament temperature calculation is coupled to the coating calculation; however, the filament temperature converges at a much greater time step than the particle calculation. Thus, the filament temperature was only calculated for every 100 time steps of the coating temperature calculations, which dramatically decreases the computation time. The filament temperature required for the particle temperature calculations was then linearly interpolated for every particle time step.
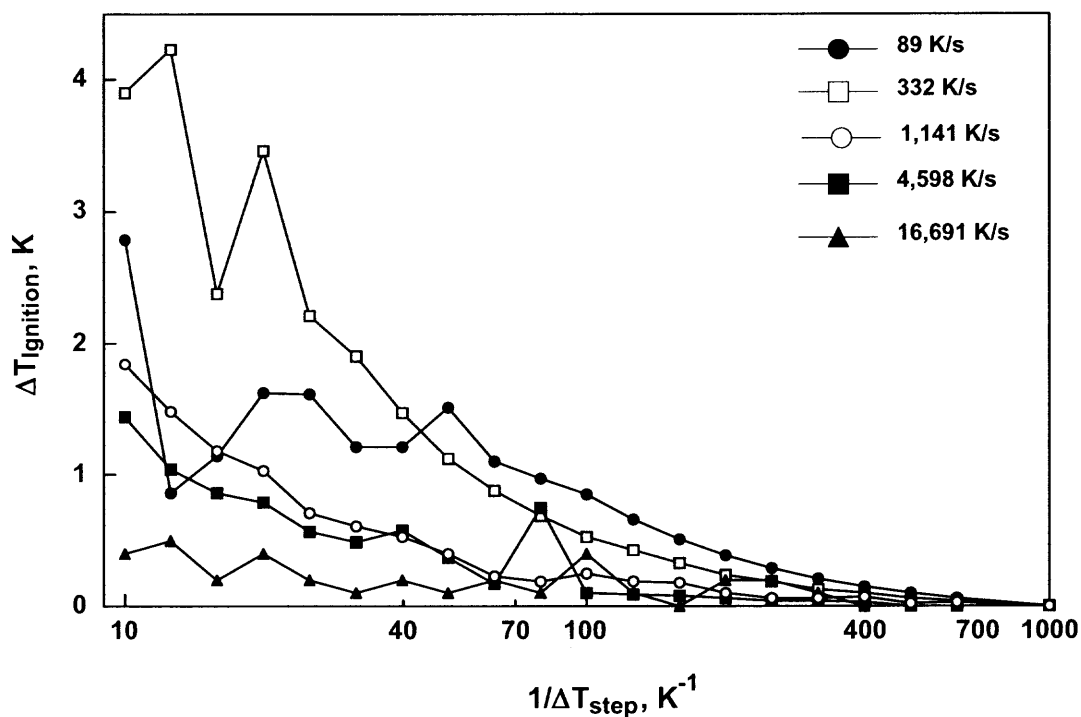
Figure 4.7 Convergence of the ignition temperature for decreasing temperature step.

4.7 Ignition Criterion

Since the model is being validated with experimental data and the calculated ignition temperatures are being compared with experimental ignition temperatures, the ignition instant in the model should reflect similar characteristics to the experimental determination of the ignition instant. In the experiments, the ignition instant is determined from the radiation emitted by the burning powder. Magnesium burns in the vapor phase so the particle temperature should be well above melting and near the boiling point. Therefore, the ignition instant is taken as the instant when the particle temperature is greater or equal to the Mg boiling point of 1363 K. The particle temperature jump near the ignition instant is very rapid since the chemical energy release is close to the exponential asymptote; so the error that could be introduced because of using this criterion as apposed to a differently defined ignition instant is well within the experimental standard deviation. The predicted ignition temperature is the temperature of the filament, located exactly where the pyrometer is focused in the experiment, at the ignition instant determined by the above criterion.

CHAPTER 5

COMPUATIONAL RESUTS

5.1 Summary ofInput Parameters

With the model equations formulated, the input parameters are summarized in Tables 5.1-5.3. The parameters in Tables 5.1-5.3 characterize the filament and powder coating's physical, transport, thermodynamic, geometric, and chemical properties. Table 5.1 represents parameters that were experimentally measured. Parameters in Table 5.2 are based on reference data. Parameters in Table 5.3 are adjustable. Parameter values based on the mean of experimental measurements indicate the standard deviation from the distribution of measurements. The experimental error is not given for some of the experimental values for which it is less than 1%.

The surrounding temperature and initial temperature of the filament and coating was fixed at 298 K. The temperature dependent properties of air such as thermal conductivity, kinematic viscosity, and Prandtl number were taken from Reference [20]. The parameters affecting the heating rate, e.g. the voltage and external resistance in the electrical circuit, are discussed in the next section since the model heating rates are tuned to match the experiment heating rates.

Table 5.1 Summary of Model Input Parameters Obtained from Experiment

Parameter	Symbol	Value
Particle diameter	d_p	9.71±5.89 µm
Layer thickness	-	55.6 µm
Mg powder thermal diffusivity	α_b	2.29±0.07 m²/s
Measured powder density	ρ_b	1259±64 kg/m³
Length of powder coating	L_c	9.5±1 mm
Pyrometer distance from coating	L_p	2 mm
Filament diameter	D_f	492 µm
Filament length	L_f	4.67 cm

Table 5.2 Summary of Model Input Parameters Obtained from Literature References

Parameter	Symbol	Value	Reference
Mg density	ρ_{Mg}	1740 kg/m³	[20]
Mg specific heat	C_p	1024 J/kg K	[20]
Activation Energy	E_A	215 kJ/mol	[4,10,24-28]
Latent Heat of Fusion	h_f	358 kJ/kg	[30]
Heat of Reaction Solid	ΔH_s	24.7x10⁶ J/kg	[29]
Heat of Reaction Liquid	ΔH_l	25.35x10⁶ J/kg	[29]
Melting Temperature	$T_{melting}$	923 K	[20]
Nichrome thermal conductivity	k_f	12 W/m K	[20]
Nichrome specific heat	$C_{p,f}$	420 J/kg K	[20]
Nichrome density	ρ_f	8400 kg/m³	[20]
Nichrome emissivity	ε	0.75	[16-19]
Nichrome resistivity	ξ	112x10⁻⁸ Ωm	[15,21,22]

Table 5.3 Summary of Model Adjustable Parameters

Parameter	Symbol	Value
Pre-exponent	Z	1x10¹⁰ kg/m²s
Mg emissivity	ε	0.75
View Factor	F	0.5
Circuit voltage, four lower heating rates and the highest	V	12.3, 24 V
Circuit resistance, lowest heating rate to highest	R_f	2.08, 1.27, 0.635, 0.18, 0.187 Ω

5.2 Filament Heating Rate Matching

Computed heating rates were matched to the experimental data by adjusting the theoretical electrical circuit voltage and external resistance. An uncoated filament was used in the experiments for the heating rate matching. The voltage for the four lower heating rates when only one battery was used to heat the filament was set to 12.3 V, in close agreement with the measured voltage. The voltage for the highest heating rate, when two batteries were connected in series, was set to 24 V. For each heating rate, the external resistance was adjusted until the computed heating rate curve fit the experimental curve in the temperature region near ignition. The resulting fits for all heating rates are shown in Figure 5.1. The scales are plotted logarithmically only for ease in viewing all heating rates. Heating rates are shown to increase from right to left. Note that the experimental temperature curves are only calibrated in the temperature range between 800 and 1250 K (shaded region), therefore, the initial portion of the all the experimental curves should be disregarded.

The experimental temperature curves shown in Figure 5.1 were obtained by comparing ten experimental curves for each heating rate and selecting the one that represented the most typical experiment. The temperature history of the filament matches well with the experimental and is within the standard deviation of the experiments, for the calibrated range of temperatures. The model's external resistance for this match is 2.08, 1.27, 0.635, 0.18, and 0.187 Ω for the lowest to highest heating rate, respectively. The predicted temperature histories for the lowest two heating rates are somewhat lower than the experimental curves at higher temperatures. This minor discrepancy could be explained by substantial oxidation of the filament occurring over

the relatively long heating times. The oxidation could reduce the emissivity of the filament resulting in somewhat higher temperatures. Such a decrease in filament emissivity was qualitatively observed: a filament heated for a long duration had a lighter surface tone than one rapidly heated. This minor discrepancy did not affect the ignition temperature measurements discussed below because ignition was observed at lower temperatures, where agreement of the calculation and experiment was good.
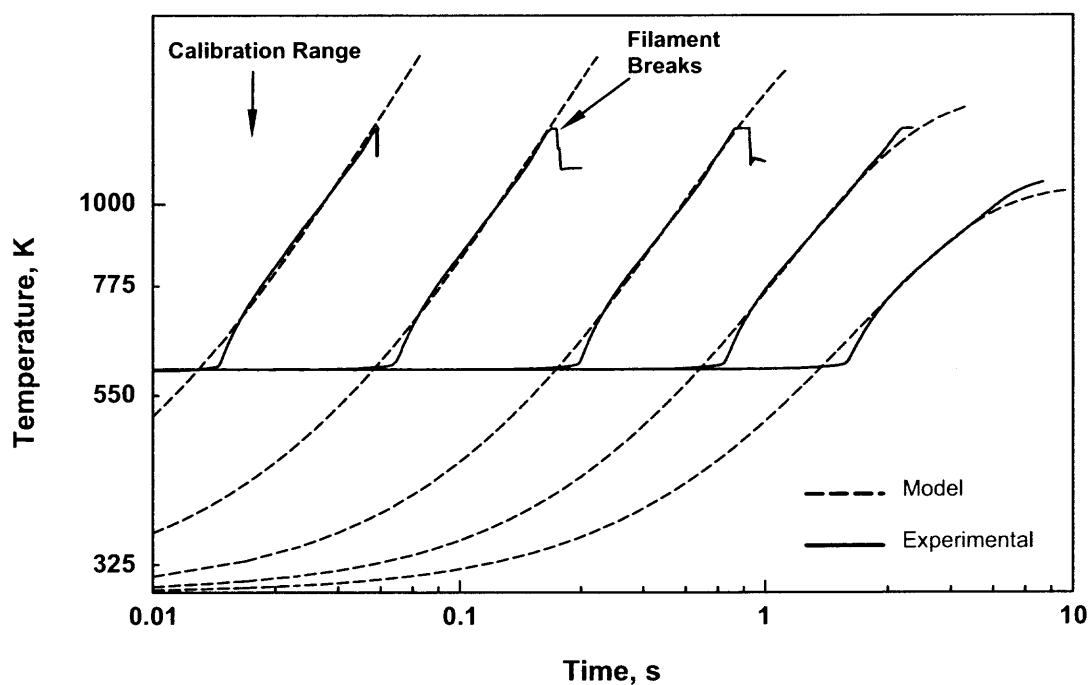
Figure 5.1 Model heating rate fit to the experimental.

5.3 Outline of Algorithm

The program structure used to solve the model equations is outlined in the algorithm flowchart illustrated in Figure 5.2. The model's differential equations were solved using a forward finite difference scheme. Because the solution is explicitly solved, the filament and particle temperature histories are solved at the current time step using the temperatures from the previous time step. The programming language implemented was MATLAB because it is matrix based and has a robust mathematical and graphical interface.

The algorithm begins with the definition of constant and adjustable parameters such as pre-exponent and particle diameter. The Nusselt number of the filament and coating are then tabulated for a temperature range of interest and fitted to polynomial functions. The heating rate loop is then set to compute one or more ignition temperatures for the respective range of heating rates.

The second algorithm block generates empty arrays for the temperature and heat transfer terms based on the filament and coating discretization parameters. This memory allocation process increases the computation speed because the software does not have to reallocate memory when arrays are augmented. The initial and boundary conditions are assigned to these arrays. The time step is also initialized with a value based on the upper time step limit of 1×10^{-4} s.

The first solving routine is for the filament equations. The filament temperatures at the next time step are calculated for all nodes in the filament mesh. This routine is only accessed every 100 particle time steps to reduce time.

The second solving routine is for the coating, where each layer temperature is individually solved based on the energy balance equations for that layer. The melting equations are also addressed in this routine using additional statements if the particle temperature is the melting temperature. An adjustable time step is used, that is based on the computed rate of temperature change. The temperature changes in this routine are monitored to ensure that a temperature jump is not greater than the ΔT_{step}. This is only a problem right after melting where the excess heat from melting causes a large increase in temperature. If the calculated temperature jump is greater than the maximum pre-set value, the loop is repeated using a smaller time step.

The next algorithm block checks to see if the ignition criterion is met, i.e., if the temperature of any particle layer in the coating is greater than or equal to the boiling point. If the criterion is satisfied, then the program flow shifts to the output block. If not, the time step is calculated using the linear adaptive method and the program flow is redirected back to the solving routines for the next time step.

The output block of the algorithm organizes the key temperatures at the ignition instant and calculates the respective heating rate that can be directly compared to the experiment. A 20 K range before ignition is used to calculate the heating rate. The parameters of interest are written to a file and the results are displayed numerically and graphically. Typically, many heating rates are calculated in one run, so this block keeps the relevant history for all the heating rates to output in one file.

The estimated computation time per heating rate is on the order of 60 s. Many of the built in functions of MATLAB were eliminated to achieve this time. There are approximately 130,000 particle time step iterations before ignition. The computation

time could be further reduced using a lower level programming language that handles loops better than MATLAB, but for development purposes, the current computation time is acceptable.

The MATLAB source code for the ignition model is provided in Appendix B.
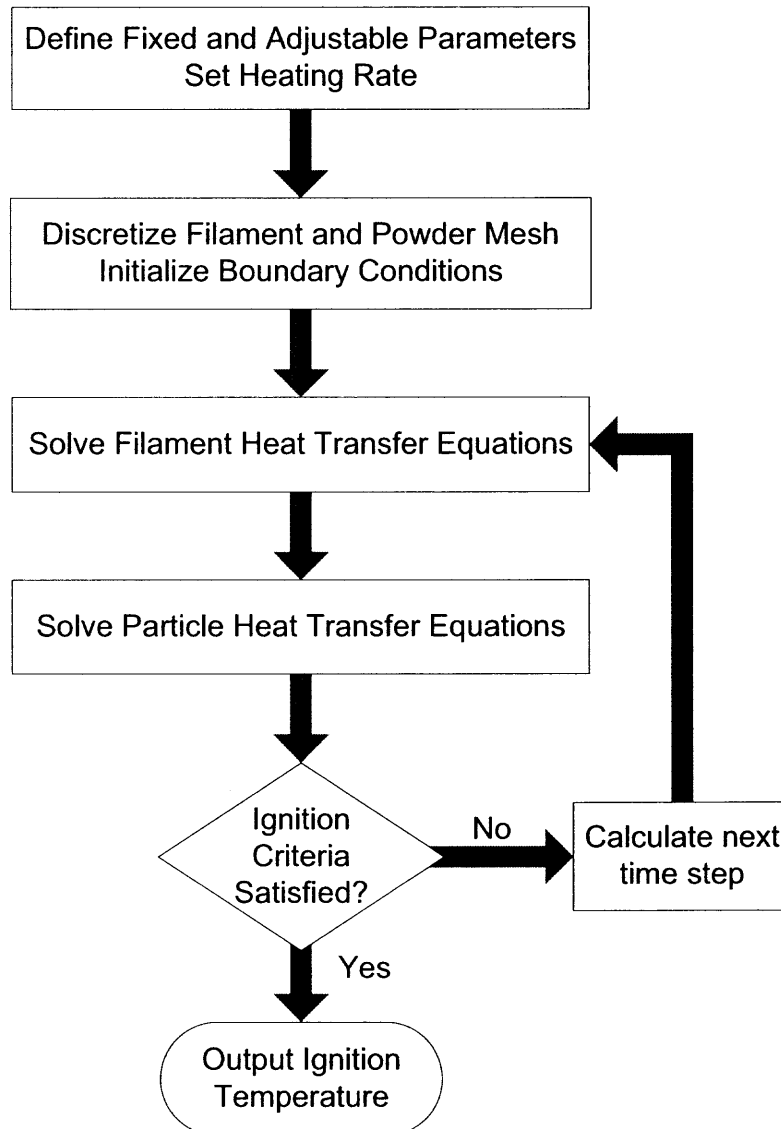
Figure 5.2 Algorithm flowchart for heat transfer model.

CHAPTER 6

RESULTS AND DISCUSSION

6.1 Ignition Experiments

Ignition temperatures for each fixed heating rate are shown in Figure 6.1. The experimental heating rates and ignition temperatures are given in Table 6.1. The heating rates are based on the slope of the filament temperature for a 20 K range before ignition. The error bars in Figure 6.1 indicate the standard deviation of the experimental distribution, which is based on ten measurements per heating rate. The experimental curve shows a nonlinear trend over the range of heating rates. To understand this trend and processes behind this kinetic data, the model results will be analyzed.
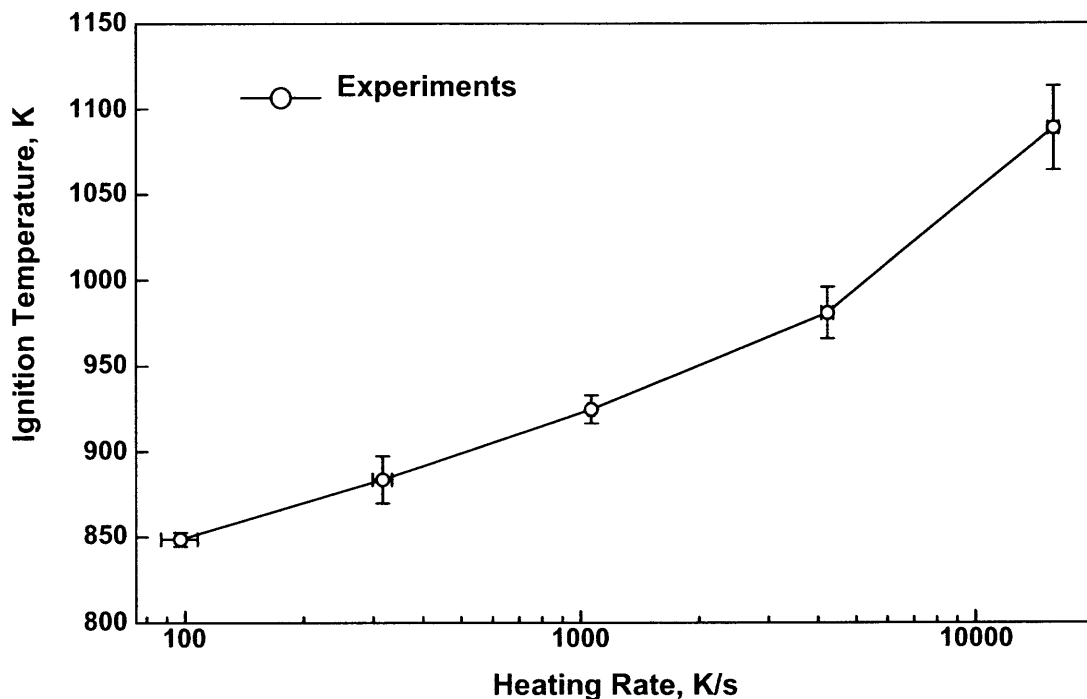
Figure 6.1 Experimental ignition temperatures as a function of heating rate.

Table 6.1 Experimental Heating Rates and Ignition Temperatures

Heating Rate, K/s	Ignition Temperature, K
97.2±10.3	848.6±4.1
316.5±17.6	883.5±13.8
1067.2±18.5	924.7±8.2
4223.7±150	981.1±15
15,724±501	1088.7±24.7

6.2 Laser Flash Diffusivity and Contact Resistance

Before the model results can be interpreted, the empirical parameters should be discussed to identify the possible error. From the three samples that were tested in the laser flash diffusivity technique, the average thermal diffusivity, α_b, for the spherical Mg powder was determined to be $2.29\pm0.07 \times 10^{-7}$ m^2/s. In comparison, the thermal diffusivity for pure Mg is 87.6×10^{-6} m^2/s [20], so the experimental value for the packed powder is 38 times less, which is reasonable considering the many contacts and packing structure. The average density, ρ_b, of the powder samples was measured to be 1259±64 kg/m^3, corresponding to a 72 % packing density. This empirical packing density is very close to the 74% packing density for hexagonal close packing suggesting that our packing structure is a reasonable assumption. However, the powder is polydispersed, so there can be small particles in the voids created by large particles thereby increasing the packing density. The corrected number of contacts is calculated to be 2.93 using Equation (4.1) and the measured bulk density. From the experimental bulk properties and the number of contacts, the contact resistance of a single particle contact is calculated to be 8.15×10^{5} K/W using Equation (4.10). One possible source of error in the contact resistance has to do with the inaccuracy of the flash diffusivity experiment because of the unaccounted heat losses. The flash diffusivity technique is designed for short heating and equilibration

times (ms range), however, longer times (s range) were used in our tests. The long times were observed because of the relatively low thermal diffusivity of the powders and because a low laser fluence was used to avoid powder melting and ignition. Thus, the heat losses to the sides of the sample could become noticeable and the time to the half of the maximum temperature could shift. This shift is currently unaccounted for in the thermal diffusivity calculation because the heat loss could not be quantified based on experimental data. The problem could be addressed using a model of the experiment and comparing the calculated heat loss to the temperature decay of the thermocouple. Yet, this shift is not expected to change the diffusivity by more than 10% and the heat loss quantification is beyond scope of this project.

6.3 Particle Temperature History

To understand the heat transfer processes leading to ignition, the particle temperature history of each layer should be examined. The complete temperature history for the igniting particle layer is shown in Figure 6.2 for each heating rate. The heating rate is shown to increase from right to left. The onset of the chemical reaction is well identified for all heating rates by the rapid temperature increase. The computed ignition temperatures for each model heating rate are given in Table 6.2. The temperature distributions within the coating at the ignition instants are shown in Figure 6.3 for the five heating rates. For the lower heating rates, the filament is observed to act like a heat sink and the outer layers ignite. Alternatively, the filament acts as a heat source at the higher heating rates and the inner layers ignite. Depending on the balance of heat losses to the environment and to the filament, ignition can occur in different layers.
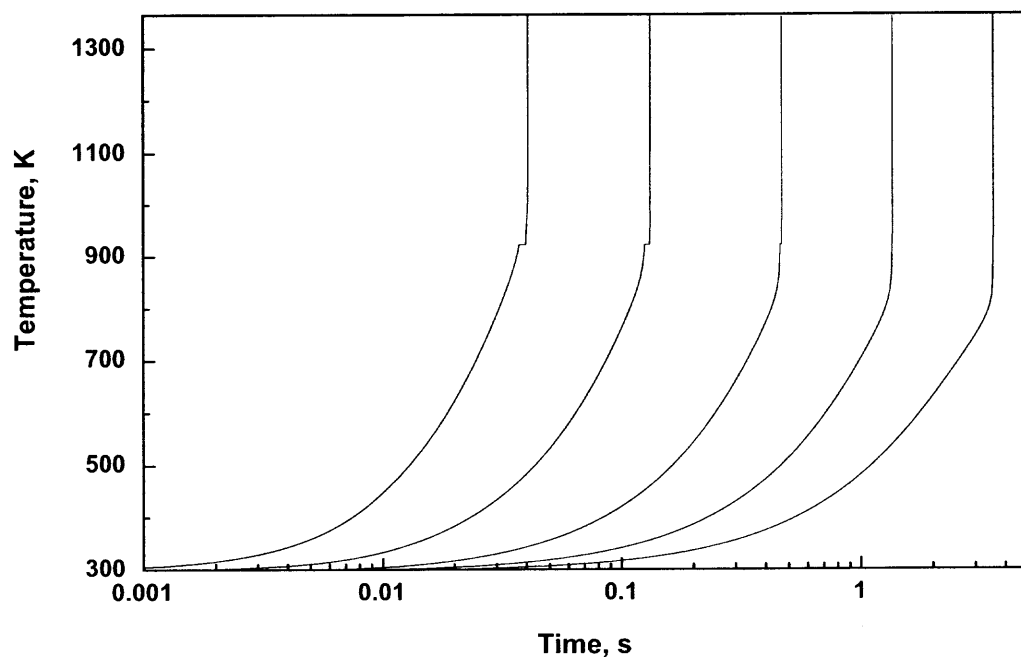
Figure 6.2 Particle temperature histories for the igniting layer for different heating rates.
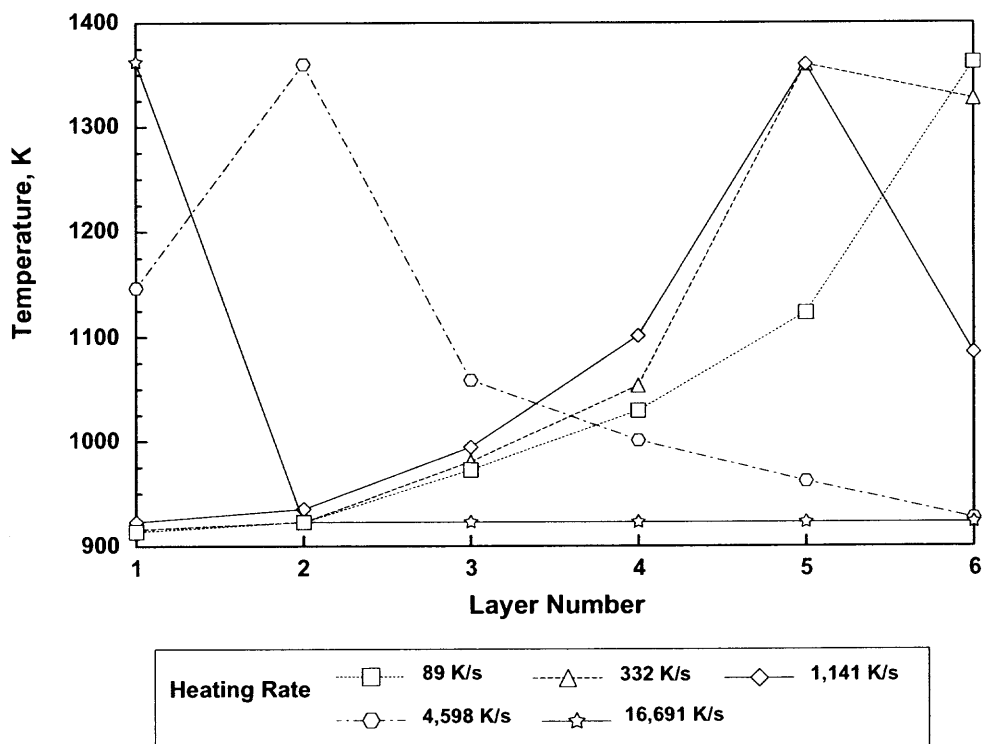
Figure 6.3 Temperature distributions within the coating at ignition for different heating rates.

Table 6.2 Computed Heating Rates and Ignition Temperatures

Heating Rate, K/s	Ignition Temperature, K
89	846.3
332	882.93
1,141	920.81
4,598	992.84
16,691	1092.1

The coating temperature history near ignition for each heating rate is illustrated in Figure 6.4. The temperature history for each layer is shown with the temperature histories of the filament at the pyrometer location, T_{pyro}, and beneath the powder, T_{coat}. In Figure 6.5, the temperate distributions along the filament for each heating rate are shown for every 90 filament time steps; note that the time steps are not equal. The heating rate progression is shown to increase in Figures 6.4 and 6.5 for plots A through E.

The observed heat transfer processes vary significantly from lowest to highest heating rate as shown in Figure 6.4 A-E. For the lowest heating rate of 89 K/s, see Figure 6.4A, all particle layer temperatures are close to the filament temperature until the chemical term becomes dominant and the layer temperatures increase above the filament temperature. Although this transition is not shown in Figure 6.4A, it occurs gradually starting at approximately 817 K. At this point, the filament begins to act as a heat sink and the coating begins to heat the filament. The particles continue to self heat until melting is observed as the isothermal process. Because the filament is a large heat sink, the first powder layer does not experience melting. The 4th and 5th layer are the first to complete melting, then the 6th layer completes melting and its temperature increases past the boiling point to be the igniting layer. The corresponding ignition temperature at this instant is the filament temperature at the pyrometer location which is 846.3 K as given in

Table 6.2. Thus, for the lowest heating rate, the losses to the filament are greater than the losses to the environment and the outer layer ignites. Observing the temperature profiles in Figure 6.5A, it is evident that the particle self heating increases the filament temperature beneath the powder layer above the temperature measured by the pyrometer, where the pyrometer location is at 0.031 m on the abscissa of Figure 6.5.

The second heating rate, 332 K/s, shown in Figure 6.4B has characteristics similar to the lowest heating rate in the sense that particle self heating brings the coating temperature above that of the filament much earlier than ignition is observed. The 5th layer is the first layer to finish melting and is the igniting layer, although the 6th layer is not far behind, as is also illustrated in Figure 6.3. The filament temperature profile for this heating rate, see Figure 6.5B, also shows significant heating by the coating.

Self heating is also the mechanism behind the particle heating for the third heating rate of 1141 K/s, as shown in Figure 6.4C. The chemical term begins to dominate at 846 K, bringing the particle layer temperature above the filament. The 5th layer is the first layer to complete melting and is the igniting layer because the filament again acts as a heat sink. Consulting Figure 6.5C, the particle self heating has little effect on the filament temperature beneath the coating.

The fourth heating rate of 4,598 K/s, shown in Figure 6.4D, has a different history than the first three heating rates. The filament temperature brings the coating temperature close to melting (901 K), and then the chemical term dominates. Furthermore, both self heating and the filament drive the melting, and every particle layer experiences melting. By the end of melting, a small temperature gradient is present between the filament and the coating, approximately 11 K. After melting is completed and the temperature of the

coating is allowed to increase, both the physical and chemical heat transfer terms rapidly increase the coating's temperature and the 2nd layer ignites first. The filament temperature plot, Figure 6.5D, indicates a 50 K temperature difference between the temperature beneath the coating and the at the pyrometer location.

The temperature history for the last heating rate, 16,691 K/s, is given in Figure 6.4E. Throughout most of the heating, the temperature gradient between the filament and the first layer, and the between layers is very large, approximately 80 K and 25 K, respectively. The rate of chemical heat release before and during melting is small compared to the filament heating rate—the filament heat drives the entire melting process. The only layer to complete melting is the 1st layer and the temperature gradient between the filament and first layer at the end of melting is approximately 100 K. This large gradient rapidly increases the physical heat and subsequently triggers the chemical term and the 1st layer ignites. The temperature difference between the filament temperature beneath the coating and at the pyrometer location is 52 K for this heating rate and is illustrated in Figure 6.5E.

Two identifiable ignition regimes have been observed for the range of heating rates selected. The change in regime occurs somewhere between the heating rates of 1,141 and 4,598 K/s. Particle heating in the first regime is driven by particle self heating since the filament behaves like a heat sink instead of a heat source. Thus, the outer particle layers are the igniting layers. Particle heating in the second regime is driven by the filament and the chemical heat contribution before and during melting is small. This becomes more evident as the heating rate increases. Furthermore, temperature gradients between layers become larger as the heating rate increases. The mechanism

distinguishing which layer ignites is simply the temperature distribution in the coating governed by the heat losses to the filament or environment.

The temperature gradient along the filament due to losses and heat gain from the coating indicate that there is some discrepancy between the pyrometer measurements and the actual filament temperature beneath the coating. However, there is no clear way to unambiguously define the ignition temperature based on the experimental data, so the pyrometer temperatures measured at the ignition instant as described above will continue to be referred as the ignition temperature.
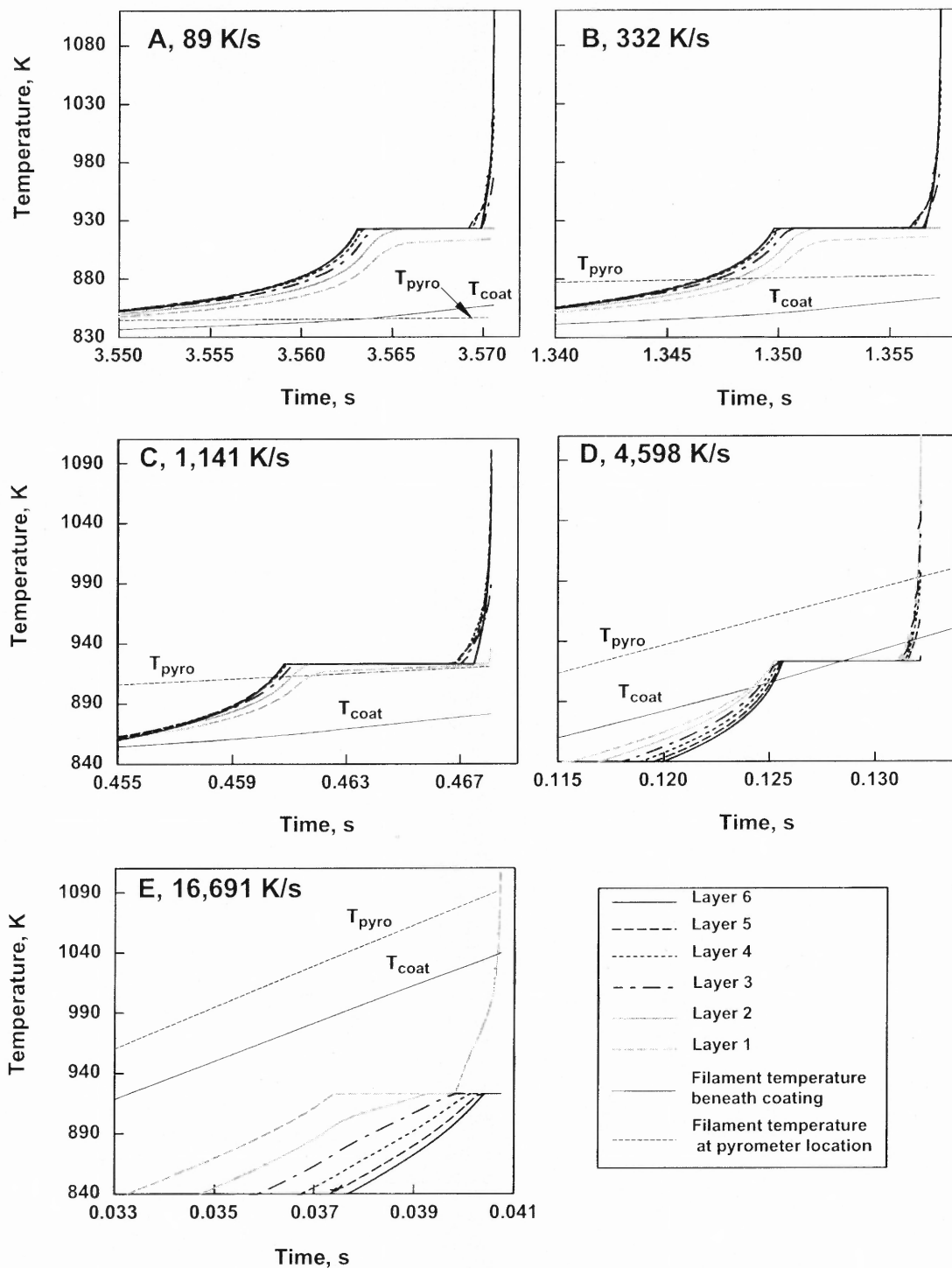
Figure 6.4 Computed and filament temperature histories for all layers near ignition.
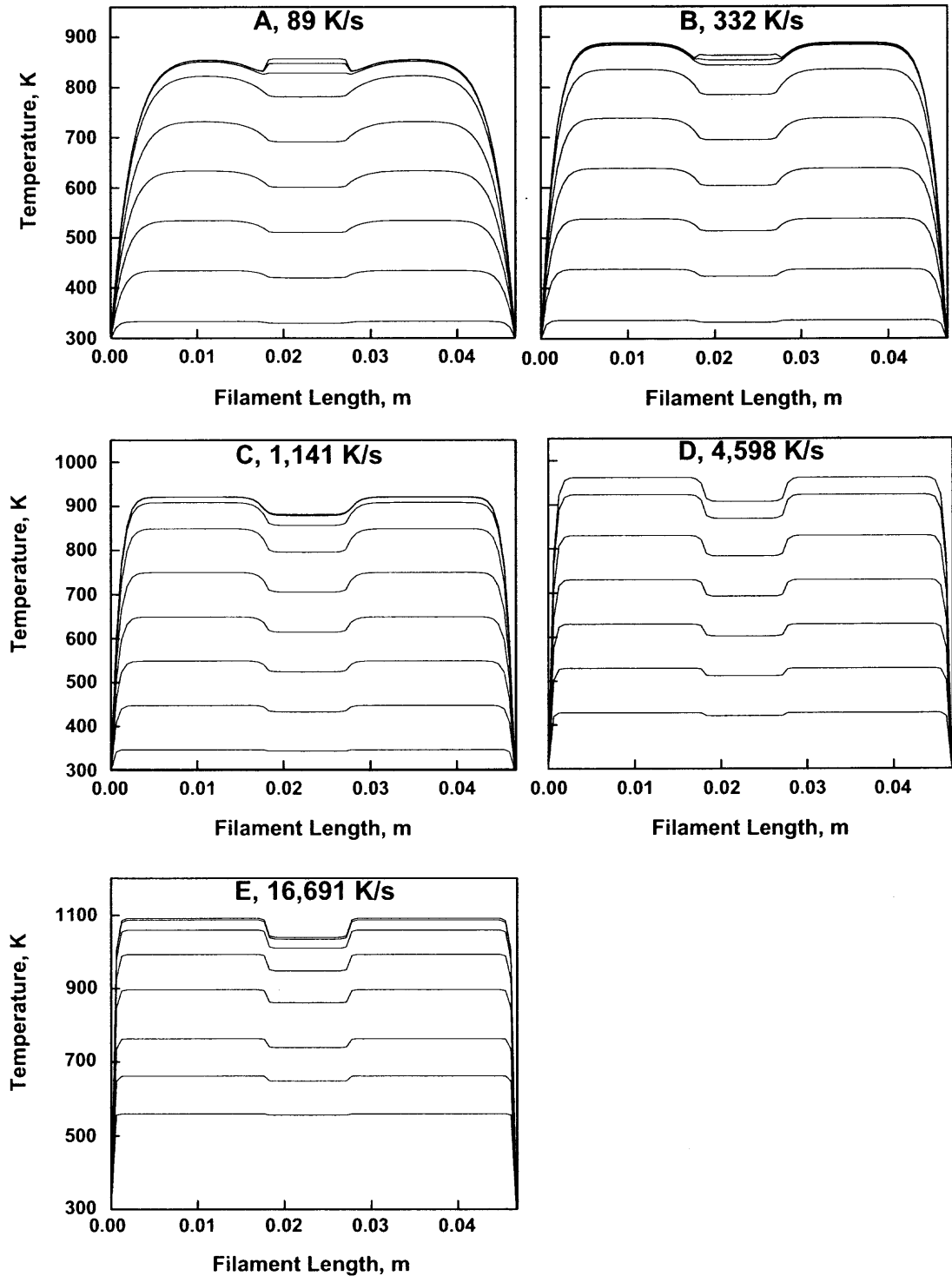
Figure 6.5 Filament temperature profile for all heating rates.

6.4 Experiment and Model Comparison

The predicted ignition temperatures (Table 6.2) are compared to the experimental ignition temperatures (Table 6.1) in Figure 6.6. The Arrhenius pre-exponent corresponding to this fit is 1×10^{10} kg/m^{2}s. The fit is quite good and within one standard deviation of experimental data points. The value of the Arrhenius pre-exponent was selected to achieve a reasonable agreement with experimental data. Further improvement of the quality of the achieved match between the experimental data and computations was possible by fine tuning the value of the pre-exponent, but was beyond the scope of this project. The achieved match for multilayer model is qualitatively better than the match obtained using a monolayer model as in Reference [10]. The goodness of the achieved match of computations and experiment implies several points. The first point is that the model assumptions are valid or have little effect on the ignition temperature. In other words, the packing structure and one dimensional assumption for the heat transfer are suitable. The second point is that the kinetics leading to ignition can be described using one Arrhenius pre-exponent factor for the range of heating rates observed. The effects of all adjustable and experimental parameters used in the model on the pre-exponent will be discussed in the next section. The last point is that the model ignition criterion is adequate for the description of the experimentally observed ignition. In future work, ignition may be explored computationally to find the exact instant and temperature when the particle becomes self heating.
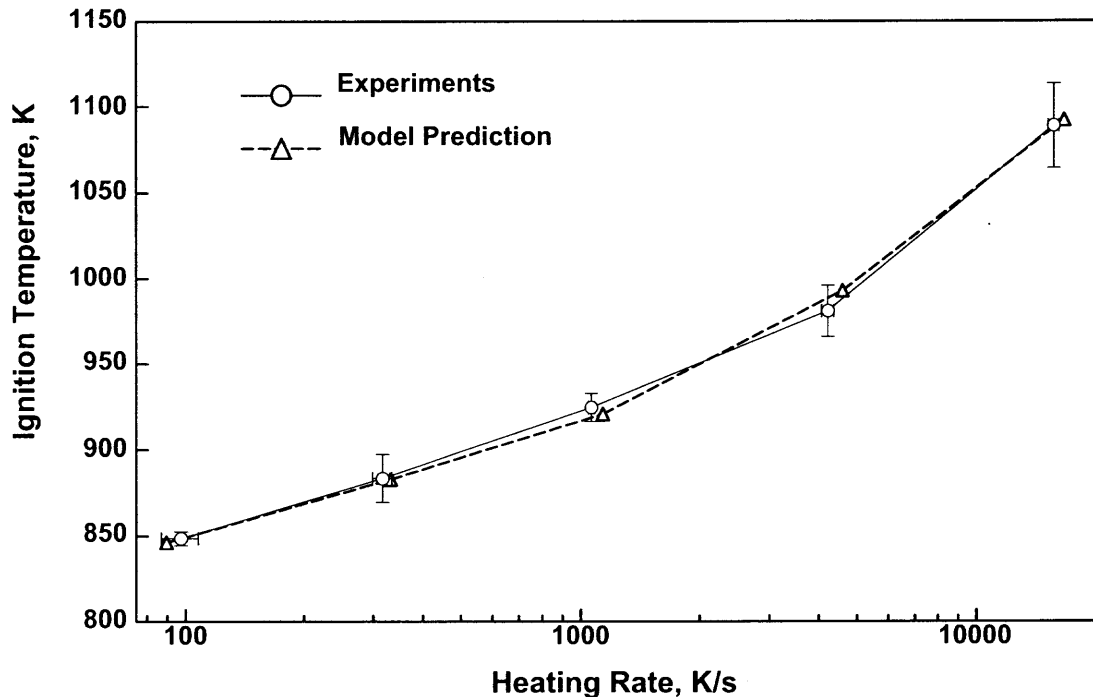
Figure 6.6 Ignition temperature comparison between model and experiments.

6.5 Model Sensitivity

To determine how different input parameters affect the ignition temperature, a sensitivity analysis was performed. By comparing the computed change in ignition temperatures for the respective parameters, the correlation among different parameters including the pre-exponent can be identified. This correlation will allow one to predict the model behavior as a function of certain parameter variations.

All input parameters that characterize the coating's thermal, geometric, and chemical properties in Tables 5.1-5.3 were selected for the sensitivity study. In general, the primary goal of this analysis is to establish the sensitivity of the model to the used powder coating parameters; thus sensitivity to the parameters used in the filament heat transfer model is not considered. The sensitivity parameters include: the pre-exponent,

number of layers, particle diameter, density, thermal diffusivity, activation energy,

coating length, pyrometer location, and number of contacts. The nominal, minimum, and

maximum values for both experimentally determined and adjustable parameters are given

in Tables 6.3 and 6.4, respectively. The parameter variations for the particle diameter,

density, and thermal diffusivity are the standard deviations from the measurements. The

variations for the coating length and pyrometer location are based on the measurement

uncertainty and the coating reproducibility. For the activation energy, the range was

based on the typical experimental error in the thermal analysis experiment and the

difference between the literature data [4,10,24-28]. Variations in the adjustable

parameters were decided so that ignition temperature changes were reasonably small to

avoid nonlinear behavior.

Table 6.3 Experimentally Determined Model Parameters Varied in the Sensitivity Study

Parameter	Nominal Value	Minimum Value	Maximum Value	Range
Particle diameter, d_p	9.71	3.82	15.6	standard deviation
Density, ρ_b	1259.7	1195.5	1323.9	standard deviation
Thermal Diffusivity, α_b	2.29×10^{-7}	2.23×10^{-7}	2.36×10^{-7}	standard deviation
Coating Length, L_c	9.5	8.5	10.5	experimental uncertainty
Pyrometer Location, L_p	30.5	29.8	31.1	experimental uncertainty
Activation Energy, E_A	215	205	225	Typical thermal analysis error

Table 6.4 Adjustable Parameters Varied in the Sensitivity Study

Parameter	Nominal Value	Minimum Value	Maximum Value	Range
Pre-exponent, Z	1×10^{10}	9×10^{9}	1.1×10^{10}	±10%, small range
Number of Layers, n	6	5	7	±1 layer, minimum range
Number of Contacts, η	2.935	2.5	3.5	Selected small range
Particle Emissivity, ε	0.75	0.65	0.85	±13%, small range
View Factor, F	0.5	0.4	0.6	±20%, small range

The ignition temperatures were calculated for each independent parameter variation and the normalized ignition temperature difference is plotted as a function of heating rate in Figures 6.7 and 6.8. The normalized temperature difference, T', is the difference between the computed ignition temperature, T_{calc}, (for the minimum and maximum values) and the baseline ignition temperature, $T_{baseline}$, that best fits the experimental data shown in Figure 6.6. T' is defined as:

$$T' = \frac{T_{calc} - T_{baseline}}{T_{baseline}} \qquad (6.1)$$

In addition to T' being plotted in Figures 6.7 and 6.8, the normalized temperature difference, T'', between the experimental ignition temperature, T_{exp}, and the baseline ignition temperature, $T_{baseline}$, is also plotted (dashed line), and is defined as:

$$T'' = \frac{T_{baseline} - T_{exp}}{T_{exp}} \qquad (6.2)$$

The curve of T'' as a function of the heating rate illustrates the quality of the match between the experimental data and the model. The curves of T' as a function of heating rate show how sensitive the model is to deviations from the selected values of different parameters. The largest temperature differences and thus, the greatest effects on

the model output are observed for the particle diameter, activation energy, and number of layers in Figure 6.7 A-C. Note the vertical scale when comparing the temperature differences and keep in mind that the relative magnitude of the deviations is strongly connected to the parameter variation, which is arbitrary for the adjustable parameters. Comparing how the values of T' and T'' depend on the heating rate one can consider how well the developed model describes the experiment. The changes in T'' do not seem to indicate a specific increasing or decreasing trend, which shows that the model describes the experimental data well in the entire range of heating rates considered. The difference between T'' and T' for the same heating rate show the sensitivity of the model to a specific parameter. The increasing or decreasing trend in T' as a function of the heating rate suggests that if a specific parameter's value increased (or decreased), the experimental data will no longer be described well by the model. In other words, the quality of the match at different heating rates will be different.

Although the activation energy variation generally represents the experimental error, large deviations are observed because it is in the exponent of the chemical heat expression. At the same time, the T' trends for different values of E_A are almost parallel to T'', showing that a similar accuracy can still be achieved for different heating rates using different values of E_A. The same is true for the variation in Z, where the values of T' are nearly constant over the range of heating rates. It can be argued that the large deviation in T' for the particle diameter is due to the poorly represented experimental standard deviation. Because this standard deviation is for the entire histogram of particle sizes in Figure 2.1, it considers both the small and large particle size fraction that is less characteristic of the peak distribution. Yet, when smaller deviations of particle size are

computed, the magnitude of T' decreases while the overall trend is conserved. It is also interesting that assuming a particle size different from the experimentally found volumetric mean size would no longer enable us to achieve an acceptable match between the experiments and computations in the range of heating rates considered.

The sensitivity of the model is smaller to the selected number of layers (see Figure 6.7C). However, similar to the effect of particle diameters, the choice of a different number of layers would result in our inability to match the experimental data in the range of the experimental heating rates.

The model sensitivity to the parameters prescribed in Figure 6.7 E-F and Figure 6.8 A-E is generally smaller and shows that a small error in view factor, particle emissivity, density, thermal diffusivity, number of contacts, coating length, or pyrometer location would not drastically change the output of the computations. The largest deviations in T' observed for the low heating rates are the view factor and emissivity, while for high heating rates, the deviation of T' is greatest for thermal diffusivity and number of contacts. Thus, radiation plays a greater role for lower heating rates and conduction through the coating is more significant at high heating rates.
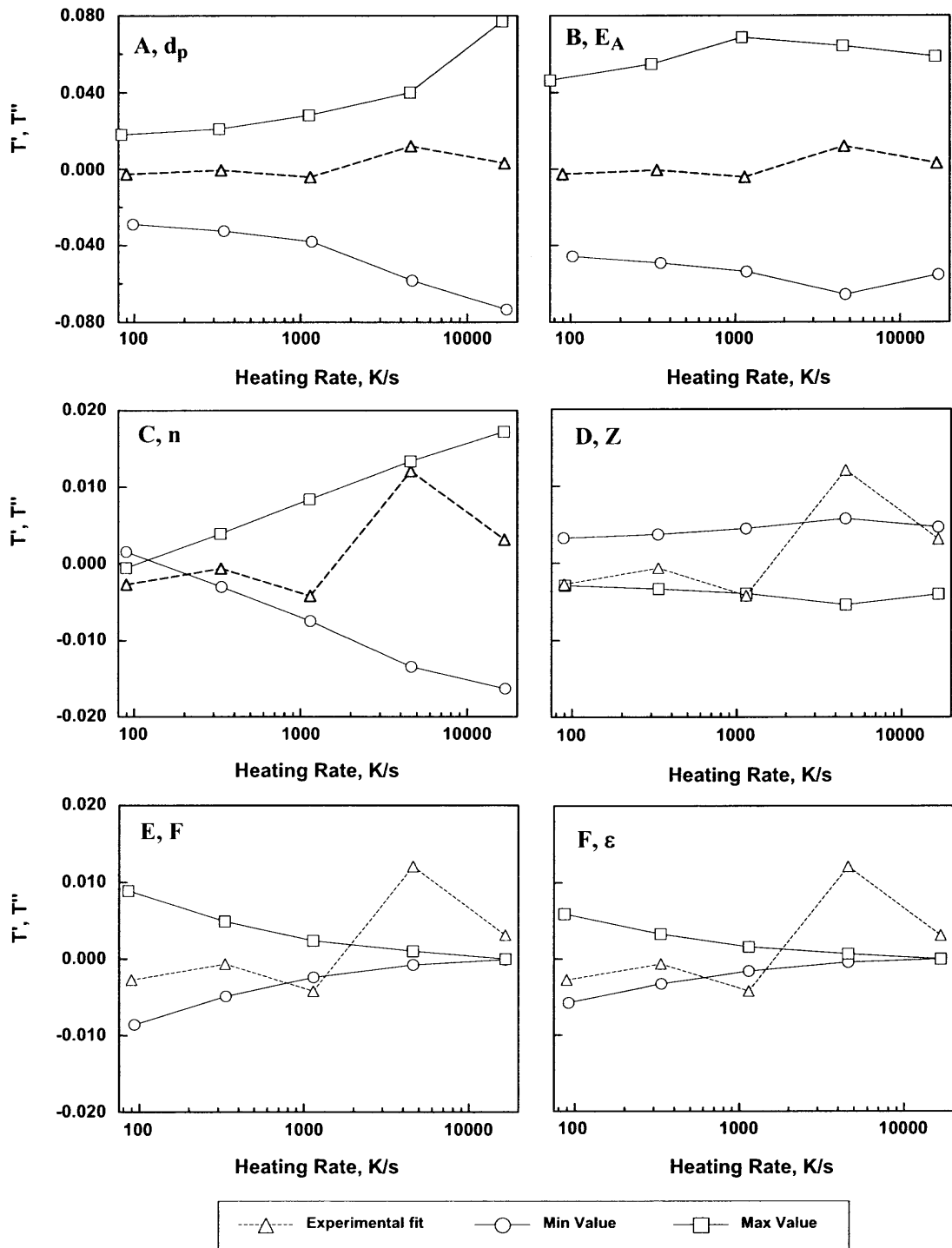
Figure 6.7 Normalized temperature differences showing sensitivity of the model to various parameters: (A) particle diameter, (B) activation energy, (C) number of layers, (D) pre-exponent, (E) view factor, and (F) emissivity.
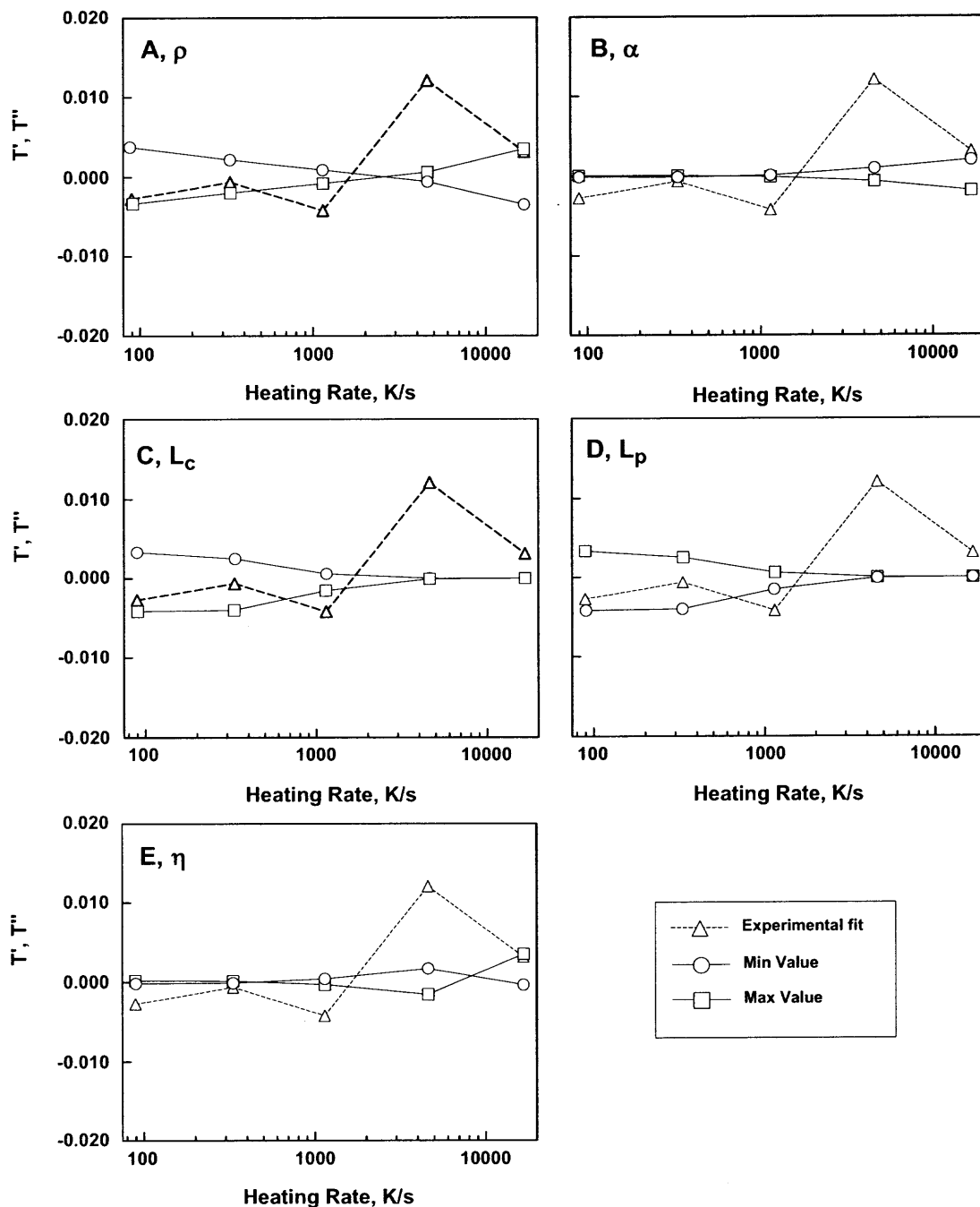
Figure 6.8 Normalized temperature differences showing sensitivity of the model to various parameters: (A) density, (B) thermal diffusivity, (C) coating length, (D) pyrometer location, and (E) number of contacts.

To determine how each independent parameter correlates with one another, a correlation matrix was created using the five heating rates as the observations. The correlation matrix is found from the covariance matrix constructed of the independent parameter vectors $\{x_1\}...\{x_n\}$, where the size of the vector is equal to the number of observations and n is the number of independent parameters. Each vector row element is the ratio between the normalized temperature difference, T'', and the fractional change in independent parameter, Y, for the observed heating rate, which is defined as:

$$Y = \frac{\Delta y}{y} \tag{6.3}$$

where Δy is the difference between the maximum and minimum parameter value, and y is the nominal baseline value for the independent parameter. Thus, the correlation is analyzed for the ratio between the relative changes in the ignition temperature and varied parameter.

The covariance matrix, C_{ij}, is defined as [31]:

$$C_{ij} = \left[\left(x_i - \mu_i \right)\left(x_j - \mu_j \right) \right] \tag{6.4}$$

where μ_i and μ_j are the means of x_i and x_j respectively. The resulting covariance matrix is a square symmetric matrix because i and j are summed over n. The symmetric correlation matrix, R_{ij}, is defined from the covariance matrix as [31]:

$$R_{ij} = \frac{C_{ij}}{\sqrt{C_{ii}C_{jj}}} \tag{6.5}$$

A null hypothesis test [31] was also performed on the correlation data to test the significance of correlation between parameters. Each value in the computed statistical significance matrix **P** is the probability of getting a correlation as large as the observed

value by random chance, when the true correlation is zero (null value). This probability is determined using the Student's t-test statistic for $N-2$ degrees of freedom, where N is the number of observations. The values in the **P** matrix, p-values, indicate the statistical significance of the correlation. The statistical significance increases as the p-value decreases. A standard significance level threshold of 5% is used in our analysis, where for $p<0.05$ the null hypothesis is rejected and the correlation is said to be significant [31]. In other words, the correlation is significant because the probability of observing the same correlation by chance is less than 5%.

The correlation **R** and significance **P** matrices are given in Tables 6.5 and 6.6 for the varied independent parameters. The statistically significant correlations in the **P** matrix (Table 6.6) are ranked as significant ($p<0.05$) or very significant ($p<0.01$), denoted by (*) or (**), respectively. For the very significant correlations, the correlating parameters are between the number of layers and the density, coating length, pyrometer location, particle emissivity, and view factor, between the particle diameter and the density and thermal diffusivity, between the coating length and the pyrometer location, and between the emissivity and the view factor. For the significant correlations, the additional correlating parameters are between the number of layers and the particle diameter and thermal diffusivity, between the density and the thermal diffusivity, coating length, pyrometer location, emissivity, and view factor, between the activation energy and the pre-exponent, between the coating length and the emissivity and view factor, and between the pyrometer location and the emissivity and view factor. For the sake of the following discussion, all values of $p<0.05$ will be considered as significant.

The above correlations can be interpreted as correlations suggested by the analytical model formulation or as correlations indicating how the numerical model describes the system. For the correlations suggested by the analytical formulation, significant correlations are anticipated because the parameters are related through one of the heat transfer expressions. A strong linear correlation between the emissivity and view factor is the result of both parameters present in the radiation Equations (4.27), (4.32), and (4.35). Hence, the radiation equations can be simplified by removing one assumed parameter. The correlation between the particle diameter, density, and thermal diffusivity is also transparent because all parameters are used to compute the contact resistance in Equation (4.10). Correlations with the particle diameter cannot be simplified because it appears in most of the heat transfer terms such as radiation, convection, and chemical. From the chemical heat generation term (Equation (4.28)), the correlation between the activation energy and the pre-exponent is obvious. The significance of this correlation suggests that for a range of activation energies a linear dependence on pre-exponent can be found, although a nonlinear correlation might better represent this correlation since both terms are related through an exponent. On the other hand, the weak correlations between the pre-exponent and all other independent parameters indicates that variations in these parameters cannot be described by varying the pre-exponent, and the pre-exponent is very specific to the experiment and the modeled powder. The significant correlation between the radiation parameters (emissivity and view factor) and the density can be explained through the energy balance Equations (4.25), (4.30) and (4.33), where the variations in these parameters balance with respect to changes in the radiation and conduction heat transfer.

The correlations reflecting how the numerical model describes the system include the correlations between parameters that are not mathematically related. These parameters are the number of layers, coating length and pyrometer location, all of which are empirically based. The significant correlation between the length parameters (coating length and pyrometer location) indicates that the outcome for any variation in either parameter is the same. In other words, the same effect on the filament temperature is observed for variations in the length parameters. The correlation between the number of layers and the particle diameter is intuitive given that a change in particle diameter changes the number of layers because of the fixed coating thickness. Varying the number of layers essentially changes the total contact resistance within the coating, thus a significant correlation between the number of layers and the density and thermal diffusivity is present by means of the contact resistance Equation (4.10). The number of layers also significantly correlates with the radiation and length parameters. At low heating rates, the amount of material on the filament, which is proportional to the number of layers, imposes the greatest temperature effect on the filament. Because similar effects regarding the amount of material and heat flow are observed at low heating rates for the radiation and length parameters, a significant correlation is evident.

The general intuitive understanding of the above correlations reinforces the validity of the model because no outlying correlations were observed that would suggest a formulation error. As in any statistical analysis, an increased number of observations would improve the strength of the presented correlations, as well as reduce the confidence interval, and should be considered in future model development. Increasing the kinetic data set to numerous heating rates would increase the strength of the

correlations and allow for more accurate extrapolation over a large range of heating rates. In addition, one could approximate the uncertainty attached to the pre-exponent as a function of each independent parameter using the given linear correlations.

Table 6.5 Correlation Matrix **R** for the Sensitivity Parameters

Number of Layers, n	Particle diameter, d_p	Density, ρ_b	Thermal Diffusivity, α_b	Activation Energy, E_A	Coating Length, L_c	Pyrometer Location, L_p	Number of Contacts, η	Particle Emissivity, ε	View Factor, F	Pre-exponent, Z	Parameter
-	0.92618	0.9721	-0.88931	0.77417	0.96213	-0.96194	0.15258	-0.96681	-0.96554	-0.79882	n
	-	0.97789	-0.99573	0.48541	0.82707	-0.82702	0.45207	-0.81432	-0.81289	-0.56981	d_p
		-	-0.95498	0.61328	0.89255	-0.89237	0.37931	-0.91102	-0.91052	-0.63897	ρ_b
			-	-0.41194	-0.78083	0.78083	-0.49551	0.75749	0.75583	0.51642	α_b
				-	0.8775	-0.87731	-0.44869	-0.86312	-0.86164	-0.93829	E_A
					-	-1	-0.02694	-0.95378	-0.95208	-0.86721	L_c
						-	0.026965	0.95343	0.95172	0.86709	L_p
							-	-0.04451	-0.04791	0.46683	η
								-	0.99997	0.8154	ε
									-	0.81168	F
										-	Z

Table 6.6 Significance Matrix **P** for the Sensitivity Parameters

Number of Layers, n	Particle diameter, d_p	Density, ρ_b	Thermal Diffusivity, α_b	Activation Energy, E_A	Coating Length, L_c	Pyrometer Location, L_p	Number of Contacts, η	Particle Emissivity, ε	View Factor, F	Pre-exponent, Z	Parameter
-	0.024*	0.006**	0.043*	0.124	0.009**	0.009**	0.806	0.007**	0.008**	0.105	n
	-	0.004**	0.000**	0.407	0.084	0.084	0.445	0.093	0.094	0.316	d_p
		-	0.011*	0.271	0.042*	0.042*	0.529	0.031*	0.032*	0.246	ρ_b
			-	0.491	0.119	0.119	0.396	0.138	0.139	0.373	α_b
				-	0.051	0.051	0.449	0.060	0.060	0.018*	E_A
					-	0.000**	0.966	0.012*	0.013*	0.057	L_c
						-	0.966	0.012*	0.013*	0.057	L_p
							-	0.943	0.939	0.428	η
								-	0.000**	0.093	ε
									-	0.095	F
										-	Z

CHAPTER 7

CONCLUSIONS

A heat transfer model was developed describing the ignition kinetics of fuel powders on a heated filament. A case study for spherical Mg powder was conducted to validate the model. The model lumps together all the exothermic processes leading to ignition into one Arrhenius type chemical heat generation term. An expression for the contact resistance between particles in the powder coating was derived as a function of the bulk properties of the coating. The bulk thermal diffusivity of the Mg powder coating was measured using the laser flash diffusivity technique to be $2.29\pm0.07\times10^{-7}$ m^2/s. The bulk packing density was measured to be 72%, which verified that a hexagonal close packed structure was a reasonable assumption for the coating packing. The filament and coating temperature histories were computed using explicit finite difference method and an energy balance approach for each node (layer) in the mesh.

The temperature histories for both the filament and coating layers indicate that during ignition the filament could act as either a heat sink or a heat source depending on the heating rate. The temperature distributions and balance of losses in the powder coating determined which of the individual layers ignited first.

The model predictions were validated with experimental results for the ignition of magnesium powder. The predictions are in good agreement with the experimental results for a range of heating rates between approximately 90 and 16,000 K/s. The Arrhenius pre-exponent corresponding to the model fit is 1×10^{10} kg/m^{2}s. For the range of heating rates examined, it is found that a single Arrhenius term can describe the exothermic

processes leading to ignition of magnesium powder. The agreement for the multilayer model is qualitatively better than a model where only a single particle layer is used with an adjustable contact resistance.

The sensitivity of model parameters on the ignition temperature was studied in order to identify the significance and correlations between parameters. Two types of correlations were found: correlations suggested by the analytical model formulation and correlations indicating how well the model describes the system. From these correlations, it is concluded that some model expressions can be simplified by combining adjustable parameters, and that no significant errors in the model appear due to unjustified correlations.

The success of this multilayer heat transfer model is that good predictions are achieved for the ignition kinetics of metal powders using experimentally determined properties of the powder. The heat transfer model developed will be the skeleton model for ignition kinetics computations for many other metal based fuels using the heated filament. It will be used to identify the kinetic parameters (activation energy and pre-exponent) and temperature histories leading to ignition for application in more advanced combustion modeling.

APPENDIX A

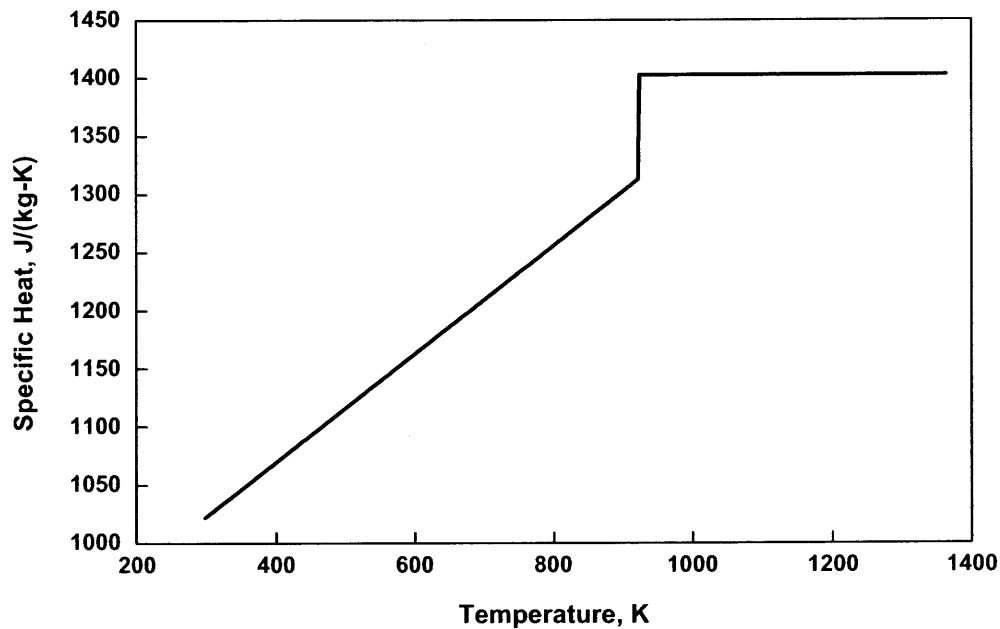## REFERENCE DATA

The figures in this appendix show the temperature dependent values for the coefficient of resistance, Nichrome specific heat, and Mg specific heat that were obtained from the literature.
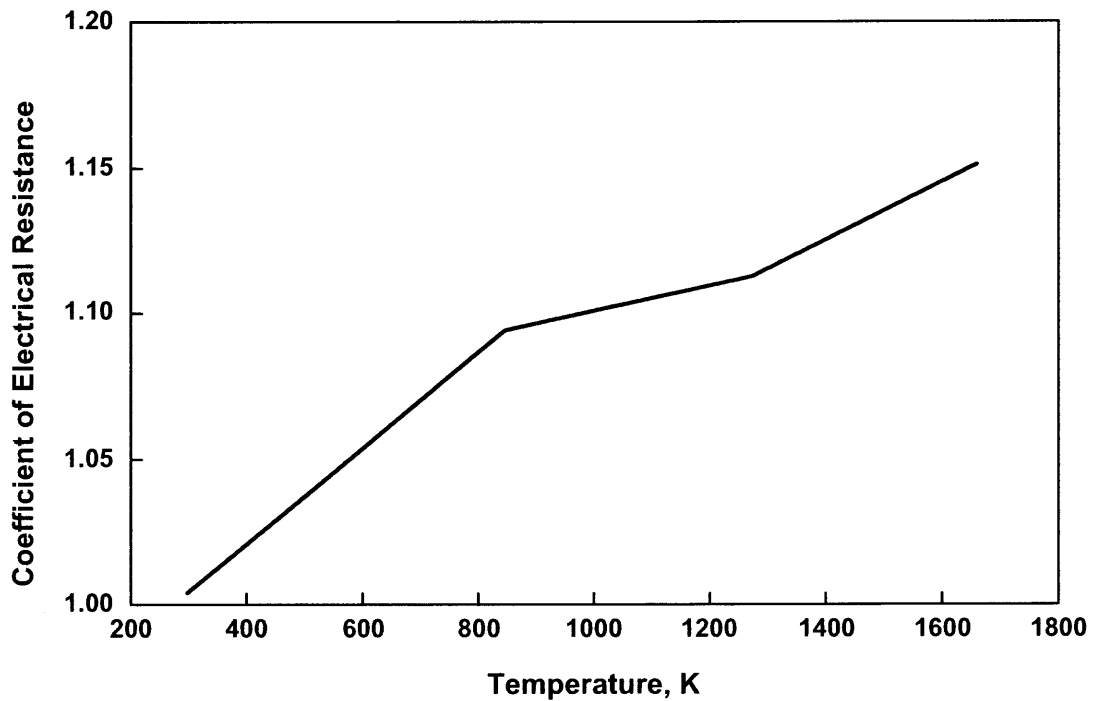
Figure A.1 Plot of the coefficient of resistance as a function of temperature for the Nichrome filament. The coefficient consists of three linear line segments based on reference data [21,22].
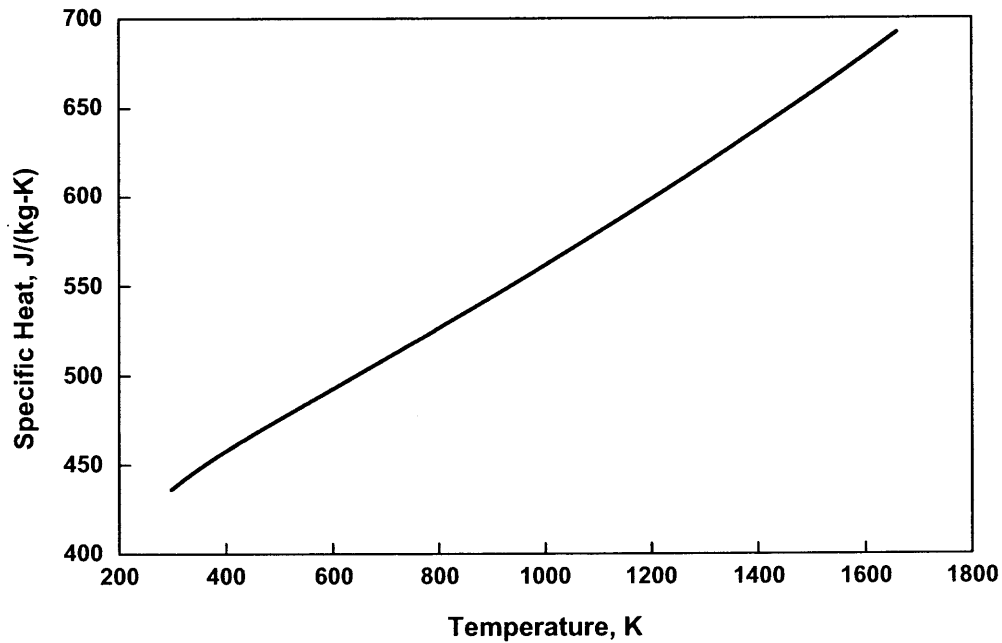
Figure A.2 Plot of condensed phase specific heat for Nichrome as a function of temperature. Specific heat values were generated for the Nichrome composition using the MTDATA software [23].

Figure A.3 Plot of condensed and liquid phase specific heat for Mg as a function of temperature. Condensed phase specific heat is approximated as a linear function given the reference data from [29]. Specific heat is constant for liquid phase.

APPENDIX B

CONTENTS OF ATTACHED COMPACT DISK

The descriptions below refer to the contents of the attached compact disk (CD). There are three main sections that include the source code used in the experimental analysis and numerical model.

A) Source Code for Experimental Ignition Analysis: In this folder, the MATLAB code is given for the data analysis of the ignition experiments. There are two files that correspond to the method used to determine the ignition instant. The first file, "low_HR_ignition.m," is the routine that determines the ignition instant based on a fixed voltage jump in the photodiode trace, which is used for the four lower heating rates. The second file, "high_HR_ignition.m," is the routine used to find the ignition instant for the highest heating rate based on the comparison between secant lines on the photodiode curve. Both files have a built in search routine to find data files saved from the experiment. The routine can be altered to open any file with a specific filename. The ignition time, ignition temperature, and heating rate are displayed for each trial.

B) Source Code to find the Half Time: This folder contains the MATLAB code, "laser_flash_diffusivity.m," to smooth the acquired data from the laser flash diffusivity experiment and locate the half time, $t_{1/2}$. The data file is specified and the thermocouple voltage data is smoothed using a Lowess method with a span of 15% of the total data points. The half time is displayed for use Equation (3.2).

C) Source Code for the Ignition Model: The MATLAB files for the ignition model are contained in this folder. The main program is "ignition_model.m" and the accompanying

function files are "Cp_part.m," "Cp_filament.m" and "resistance_coefficient.m." If you wish to run this program, place all the files in the same directory and run the "ignition_model.m" file to compute the ignition temperatures. The parameters in the program file are set for the match between the experiment and model as shown in Figure 6.6. One can adjust any of the input parameters to see the effect on the computed ignition temperature. The program is setup to compute the five heating rates in one run. The *HR* and *external_resistance* variables can be changed to compute ignition temperatures for any heating rate. The computed results are displayed on the screen and written to a file.

REFERENCES

1. Rogers, R. N. (1975). Thermochemistry of Explosives. *Thermochimica Acta, 11* (2), 131-139.

2. Pickard, J. M. (2002). Critical Ignition Temperature. *Thermochimica Acta, 392-393,* 37-40.

3. Fox, T. W., Te Velde, J. A., & Nicholls, J. A. (1976). Shock wave ignition of metal powders. *Proceedings of the Heat Transfer and Fluid Mechanics Institute,* 241-56.

4. Roberts, T. A., Burton, R. L., & Krier H. (1993). Ignition and Combustion of Aluminum/Magnesium Alloy Particles in Oxygen at High Pressures. *Combustion and Flame, 92* (1-2), 125-43.

5. Krier, H., Burton, R. L., Spalding, M. J., & Rood, T. J. (1998). Ignition dynamics of boron particles in a shock tube. *Journal of Propulsion and Power, 14* (2), 166-172.

6. Trunov, M. A., Schoenitz, M., & Dreizin E. L. (2003). Ignition of Al-Mg MechanicalAlloys. *Chemical and Physical Processes in Combustion,* 313-316.

7. Mohan, S., Trunov, M. A., & Dreizin, E. L. (2003). Characterization of Aluminum Powder Ignition. *Chemical and Physical Processes in Combustion,* 329-332.

8. Shoshin, Y. L., Trunov, M. A., Zhu, X., Schoenitz, M., & Dreizin, E. L. (2004). Ignition of Aluminum-Rich Al-Ti Mechanical Alloys in Air. Submitted to *Combustion and flame.*

9. Trunov, M. A., Schoenitz, M., & Dreizin, E. L. (2005). Ignition of Aluminum Powders under Different Experimental Conditions. *Propellants Explosives and Pyrotechnics, 40* (1), 36-43.

10. Trunov, M. A., Schoenitz M., & Dreizin, E. L. (2003). Ignition of Al-Mg Mechanical Alloys. *Proceedings of the Ninth International Workshop on Combustions and Propulsion, Lerici, La Spezia, Italy.*

11. Parker, W. J., Jenkins, R. J., Butler, C. P., & Abbott, G. L. (1961). Flash Method of Determining Thermal Diffusivity, Heat Capacity, and Thermal Conductivity. *Journal of Applied Physics, 32* (9), 1679-1684.

12. Dreizin, E. L., Berman, C. H., & Vicenzi, E. P. (2000). Condensed-phase modifications in magnesium particle combustion in air. *Combustion and Flame,* 122, 30-42.

13. Dreizin, E. L. & Hoffmann V. K. (1999). Constant Pressure Combustion of Aerosol of Coarse Magnesium Particles in Microgravity. *Combustion and Flame,* 118, 262-280.

14. Koch, E. C. (2002). Metal-fluorocarbon-pyrolants IV: Thermochemical and combustion behaviour of magnesium/Teflon/Viton (MTV). *Propellants, Explosives, Pyrotechnics, 27* (6), 340-351.

15. Arcor Electronics, Inc. (2003). Nickel Chromium Resistance Wire. Retrieved April 30, 2003, from
    http://www.arcorelectronics.com/uninsulatedwire/nickelchromium.html.

16. Kugai, V.I. (1975). Determination of the Effective Emissivity of Nichrome Wire Spirals. *Teplofizika I Optimizatsiya Teptovykh Protsessov, 1,* 72-75. (In Russian).

17. Mikron Instrument Company, Inc. (2004). Table of emissivity of various surfaces. New Jersey. Retrieved April 30, 2003, from http://www.mikroninfrared.com.

18. OMEGA Engineering, Inc. (1996). Table of Total Emissivity. Retrieved April 30,2004, from http://ib.cnea.gov.ar/~experim2/Cosas/omega/emisivity.htm.

19. Everest Interscience, Inc. (2004). Emissivity of Total Radiation for Various Metals. Retrieved January 20, 2004, from
    http://www.everestinterscience.com/info/emissivity/emissivitytable.htm.

20. Cengel, Y .A. (2003). *Heat Transfer, A Practical Approach* (2nd ed.). New York: McGraw-Hill.

21. Hyndman Industrial Products, Inc. (2003). Alloy Data Table-Resistance Heating Wire Nickel-Chromium Alloy 69% Nickel/16% Chromium-N6. Indiana.

22. Ness Engineering, Inc. (1999). Ness Engineering Technical Data-Metal/ Alloy Resistivity. Retrieved April 30, 2003, from
    http://home.san.rr.com/nessengr/techdata/metalresis.html.

23. Davies R. H., Dinsdale A. T., Gisby J. A., Robinson J. A. J., & Martin S. M. (2002). MTDATA - Thermodynamics and Phase Equilibrium Software from the National Physical Laboratory. *CALPHAD, 26* (2), 229-271.

24. .Khaikin, B. I., Bloshenko, V. N., & Merzhanov, A. G. (1970). Ignition of metal particles. *Fizika Goreniya i Vzryva, 6* (4), 474-88. (In Russian).

25. Fedorov, A. V., & Gosteev, Y. (1998). A Physical-mathematical investigation of magnesium particle ignition. *Archivum Combustionis, 16* (3-4), 137-152.

26. Fedorov, A. V. (1996). Numerical and analytical investigation of ignition of magnesium particles. *Fizika Goreniya i Vzryva, 32* (1), 75-84. (In Russian).

27. Cassel, H. M., & Liebman, I. (1963). Combustion of Mg particles. II. Ignition temperatures and thermal conductivities of ambient atmospheres. *Combustion and Flame, 7* (1), 79-81.

28. Ezhovskii, G. K., & Ozerov, E. S. (1977). Ignition of powdered magnesium. *Fizika Goreniya i Vzryva, 13* (6), 845-52. (In Russian).

29. Linstrom, P. J., & Mallard, W. G. (Eds.). (2003). *NIST Chemistry WebBook. NIST Standard Reference Database Number 69.* Retrieved November 1, 2004, from http://webbook.nist.gov.

30. Lide, D. R. (Ed.). (2001). CRC handbook of chemistry and physics (82nd ed.). Boca Raton, Florida: CRC Press LLC.

31. Zwillinger, D. (Ed.). (2003). CRC standard mathematical tables and formulae (31st ed.). Boca Raton, Florida: Chapman and Hall/CRC Press LLC.